



Cite this article: Anné J et al. 2014

Synchrotron imaging reveals bone healing and remodelling strategies in extinct and extant vertebrates. *J. R. Soc. Interface* **11**: 20140277.
<http://dx.doi.org/10.1098/rsif.2014.0277>

Received: 15 March 2014

Accepted: 15 April 2014

Subject Areas:

biochemistry, biomaterials, chemical biology

Keywords:

SRS-XRF, archosaur, histology, bone, fracture healing

Authors for correspondence:

Phillip L. Manning

e-mail: phil.manning@manchester.ac.uk

Roy A. Wogelius

e-mail: roy.wogelius@manchester.ac.uk

Electronic supplementary material is available at <http://dx.doi.org/10.1098/rsif.2014.0277> or via <http://rsif.royalsocietypublishing.org>.



Royal Society Publishing

Synchrotron imaging reveals bone healing and remodelling strategies in extinct and extant vertebrates

Jennifer Anné¹, Nicholas P. Edwards¹, Roy A. Wogelius¹, Allison R. Tumarkin-Deratzian², William I. Sellers³, Arjen van Veelen¹, Uwe Bergmann⁴, Dimosthenis Sokaras⁵, Roberto Alonso-Mori⁵, Konstantin Ignatyev⁶, Victoria M. Egerton¹ and Phillip L. Manning¹

¹School of Earth, Atmospheric and Environmental Sciences, University of Manchester, Williamson Building, Oxford Road, Manchester M13 9PL, UK

²Department of Earth and Environmental Science, Temple University, Philadelphia, PA 19122, USA

³Faculty of Life Sciences, University of Manchester, Manchester M13 9PL, UK

⁴SLAC National Accelerator Laboratory, Linac Coherent Light Source, Menlo Park, CA 94025, USA

⁵SLAC National Accelerator Laboratory, Stanford Synchrotron Radiation Lightsource, Menlo Park, CA 94025, USA

⁶Diamond Light Source, Didcot OX11 0DE, UK

Current understanding of bone healing and remodelling strategies in vertebrates has traditionally relied on morphological observations through the histological analysis of thin sections. However, chemical analysis may also be used in such interpretations, as different elements are known to be absorbed and used by bone for different physiological purposes such as growth and healing. These chemical signatures are beyond the detection limit of most laboratory-based analytical techniques (e.g. scanning electron microscopy). However, synchrotron rapid scanning-X-ray fluorescence (SRS-XRF) is an elemental mapping technique that uniquely combines high sensitivity (ppm), excellent sample resolution (20–100 µm) and the ability to scan large specimens (decimetre scale) approximately 3000 times faster than other mapping techniques. Here, we use SRS-XRF combined with microfocus elemental mapping (2–20 µm) to determine the distribution and concentration of trace elements within pathological and normal bone of both extant and extinct archosaurs (*Cathartes aura* and *Allosaurus fragilis*). Results reveal discrete chemical inventories within different bone tissue types and preservation modes. Chemical inventories also revealed detail of histological features not observable in thin section, including fine structures within the interface between pathological and normal bone as well as woven texture within pathological tissue.

1. Introduction

The morphological characterization and description (histological analysis) of extant bone is used in the comparative interpretation of extinct vertebrates often providing evidence for physiological properties such as age, reproduction, healing strategies and metabolic rates [1–5]. Histological analysis of fossil material can also aid in determining taphonomic alteration through the identification of crystal growth replacement within bone tissue [5–7]. However, in order to obtain a more complete understanding of what original details remain in fossil bone, it is important to distinguish between biologically derived constituents (endogenous material) and taphonomic artefacts added during fossilization of extinct organisms.

Although structural morphology can be preserved in a fossil despite mineral replacement, the current paradigm suggests that the original biochemical composition has been lost [6–10], with some exceptions concerning the high durability of enamel [9–13]. Recent studies, however, have shown that

endogenous chemistry can survive in even the most fragile of tissues such as rare fossils of skin [14]. Many conventional techniques have mapped soft tissue preservation in fossils and determined that these preserved tissues are chemically different from the matrix, i.e. not just impressions [14–20]. If such delicate tissues can preserve endogenous biomarkers, then it is likely that hard tissues such as bone may also contain endogenous trace elements that are critical to hard tissue mechanical properties and physiology [21].

The chemistry of original bone apatite is often defined as hydroxyapatite, but is more complex owing to the multiple substitutions that can occur within the apatite structure [8,22,23]. The ability of bone to substitute a wide range of elements makes it an important sink for trace elements essential to various physiological functions, such as fracture healing [1,24–27]. Because the rate and strategy of fracture healing are heavily dependent on physiological factors such as metabolism, nutritional status and immune response [1,21,28–30], it may be possible to use fracture healing as means to interpret physiology in extinct and extant taxa.

To fully understand the biosynthetic pathways employed by vertebrates in bone maintenance and repair, knowledge of the trace element inventory of bone is crucial. Specific trace elements such as copper, zinc and strontium have been shown to have profound impacts on bone physiology [31–35]. These elements are elevated around an affected area during the distinct stages of fracture healing allowing for the possibility of using trace elements as biomarkers for diagnosing the degree of callus maturation. Zinc has been found to stimulate bone formation and is usually correlated with areas of active ossification [31,32,36,37]. The addition of extraneous strontium increases osteoblastic activity and inhibits osteoclast proliferation and differentiation [31,32] resulting in an increase in bone deposition. This has made strontium the most studied of the trace elements related to fracture healing owing to its potential as a drug (strontium renelate, SR) to help treat osteoporosis [31,32]. Unlike zinc and strontium, copper is important for the organic constituent of bone as it is essential in the formation of cross-links found in collagen [35,38], which prevent the unravelling of the collagen protein chains. However, the distribution and dilute concentrations of key trace elements that are crucial to maintaining healthy bone are difficult to map within discrete biological structures. The advent of synchrotron-based imaging of biological and palaeontological samples is helping address these issues [17–20].

Synchrotron rapid scanning-X-ray fluorescence (SRS-XRF) combines high sensitivity (concentrations of ppm) with excellent sample resolution (from 20 to 100 µm) and the ability to scan large specimens (100 × 100 × 30 cm and up to 25 kg) almost 3000 times faster than other acquisition techniques [16–20]. SRS-XRF has been optimized to allow multi-element mapping and can also be combined with X-ray absorption spectroscopy (XAS) [17–20,39,40]. This allows for the determination of the atomic coordination of a particular element (how it is bound to other elements). This is important when determining whether or not an element is organic or inorganic in origin and thus whether it should be attributed to the tissue or to taphonomic processes [17–20].

Previous studies have used SRS-XRF coupled with XAS to examine iconic fossils such as *Archaeopteryx* [17] as well as exceptionally preserved fossils from the Green River Formation, USA [14,18,20]. In these studies, SRS-XRF of fossils

has revealed biological structures that cannot be observed in visible light as well as the fractionation of elements within discrete biological structures that can be compared with comparable tissue in living organisms. Such studies have led to the identification of specific elemental biomarkers such as eumelanin [19].

Given the propensity for trace metals mediating crucial enzymatic reactions during syntheses of extant tissues, it is important to identify if similar controls during bone genesis can be identified in fossil material. In this study, we use SRS-XRF coupled with XAS to determine the elemental composition and variation in concentrations in pathological and normal bone from both an extant and extinct archosaur (*Cathartes aura* and *Allosaurus fragilis*). Theropods are a logical study group as they are more closely related to the most diverse group of extant archosaurs, the birds. The extant avian homologue potentially provides great insights into the biology, biochemistry and physiology of their extinct dinosaur ancestors.

2. Methods

The techniques used in this study included both standard morphological and histological approaches to the preparation and analysis of extant and extinct samples.

2.1. Specimens

A distal pedal phalanx (digit III-3) of the Late Jurassic theropod dinosaur *A. fragilis* (UMNH 6282; Morrison Formation, Cleveland-Lloyd Quarry, UT, USA) was used in this study. This specimen exhibits a smooth callus on the external dorsal surface.

A proximal-most phalanx of the lateral toe (digit IV-1) of an extant turkey vulture, *C. aura* (DMNH 83356), was used for comparison. The external surface of the plantar-distal end of the phalanx is almost entirely covered with reactive bone, thereby giving a frothy appearance.

2.2. Thin section preparation

All histological analysis was performed using the thin section facilities of the Department of Earth and Environmental Science at Temple University (PA, USA). Thin section specimens from the *A. fragilis* and *C. aura* specimens were prepared by cutting along the paramedian plane through the callus for histological analysis. To prevent fracturing and flaking of the fossil, the specimen was vacuum impregnated with Paleobond penetrate stabilizer (PB002) before grinding billets down to the desired thicknesses of 100–120 µm [41]. Thin sections were viewed in both plane and cross-polarized light using a Nikon ECLIPSE E600 POL microscope and ACT-1 software. Histological data were compared with elemental data obtained from SRS-XRF to identify any associations between bone tissue types and specific elemental signatures.

2.3. Elemental mapping

Both *A. fragilis* and *C. aura* were analysed at the Stanford Synchrotron Radiation Lightsource (SSRL, CA, USA) on wiggler beamline 6-2. This beamline is one of the few facilities that can provide large-scale SRS-XRF, which allows for the rapid mapping of large sample surface areas and is preferred when first assessing the overall elemental distribution of larger specimens. The *A. fragilis* section was also analysed at the microfocus beamline, I-18, at the Diamond Light Source (DLS, Oxford, UK). The area of interest that can be imaged on this beamline provides a smaller, but higher resolution scan than the facilities of SSRL

beamline 6-2, which allows us to concentrate on areas of interest such as the interface between pathological and normal bone.

2.3.1. Stanford Synchrotron Radiation Lightsource

Specimens were mounted on an $x-y-z$ motor-controlled stage and moved in a raster pattern relative to the fixed incident beam [17–19]. Experiments consisted of an incident beam energy either at 13.5 keV for heavier (high-Z) elements (Ca and heavier) and or at 3.15 keV for lighter (low-Z) elements (Ca and lighter). Flux was calculated to be between 10^{10} and 10^{11} photons s^{-1} at high Z, and approximately 10^9 photons s^{-1} at low Z. Beam diameters of 50 μm were used for high-Z elements and 100 μm for low-Z scans. For high-Z maps, specimens were analysed under ambient conditions and aligned at a fixed incident angle of 45° relative to the beam with the single element drift detector (Vortex) set at a 90° scattering angle to the incident beam. For low-Z maps, the specimen was placed in a helium-purged sample chamber, and the scattering angle was changed to 160° to minimize signal loss. The helium atmosphere is necessary to avoid X-ray absorption and scattering effects of air that can attenuate the beam at lower incident beam energies [17].

XRF energies of interest were assigned to the detector to capture specific emission energies (up to 16 simultaneous element windows) simultaneously during mapping. To obtain rapid scanning, a full energy-dispersive X-ray spectrum is not recorded for each pixel [20]. The element windows are selected by collecting a raw energy-dispersive X-ray spectrum from 10 to 20 raster lines over an area of the map containing the majority of the different materials present in the sample (e.g. matrix, soft tissues and hard tissues) [17–20]. The averaged spectrum is used to assign the elemental windows (e.g. CaK α , ZnK α , BaL α , etc.), so that all elements are chosen based on their dominance within the energy-dispersive X-ray spectrum (electronic supplementary material). The imaging software IMAGEJ [42] was used to calculate spatial correlations from maps using the IMAGE CORRELATIONJ plugin [43].

To quantify the concentrations of elements within a sample, point analyses were selected by locating an area of interest within the scan, driving the stage to the point coordinates and collecting a full energy spectrum for 50 s (electronic supplementary material, figures S1 and S2). Three point analyses for high-Z (Ca and heavier) and two for low-Z (Ca and lighter) scans were taken at each area of interest and averaged to account for sample heterogeneity (electronic supplementary material, figures S1 and S2). Only two scans were taken at low Z owing to the constraint of experimental time available. The software package PyMCA [44] was used to fit point spectra based on the raw energy-dispersive X-ray spectroscopy files and from the experimental parameters using a Durango apatite standard of known element concentrations for calibration (electronic supplementary material) [17–20].

X-ray absorption near-edge structure (XANES) of the *Allosaurus* phalanx was conducted in fluorescence mode by scanning the incident beam energy through the sulfur K edge to determine sulfur speciation [17,19,20]. Calibration of the beam energy for XANES analyses was accomplished using a K_2SO_4 standard. XANES is particularly important to undertake on fossil samples given it helps identify the endogenous and exogenous facets of the sample. Thus, XANES was not performed on the modern bones, given that the endogeneity of the sample was not in question.

2.3.2. Diamond Light Source

Scans were undertaken at the microfocus beamline I18 using a 6.5 μm diameter pinhole with an incident beam energy of 16.5 keV to pick up the SrK α emissions (flux 10^{10} to 10^{11} photons s^{-1}). The sample was mounted on an $x-y-z$ stage and rastered at a 45° angle to the incident X-ray beam with a single element drift detector (Vortex) set to 90° scattering angle. Windows are assigned to the detector post-data collection as a full spectrum is collected for each

pixel. Maps were processed using the ROI tool in PyMCA [44]. Point analyses were selected from individual spectra within ROI maps.

The experimental set-up at DLS allows for the full extended X-ray absorption fine structure (EXAFS) to be performed. Zinc EXAFS of the *Allosaurus* material was conducted to determine whether the bonding coordination was comparable with that of hydroxyapatite (bone). EXAFS was fitted using the DEMETER software package [45].

3. Results

3.1. *Allosaurus fragilis* (UMNH 6282)

Two smooth calli are identified optically by changes in bone tissue orientation as observed under plane polarized light (figure 1): a large callus on the dorsal surface (major callus) and a smaller callus on the ventral surface. A post-mortem crack is present running from the distal-to-ventral surfaces, which appears as a void in the map of iron. In figure 1a,c, the interface between the pathological and normal tissue is labelled as a black (figure 1a,b) or red (figure 1d,e) line. The major callus is highly remodelled as shown by the maturity of the compacted cancellous tissue of the callus seen in both the optical observation of the histology (figures 1b and 2a) and in the map of iron and strontium (figures 1e and 2b, respectively). A medullary cavity is present in the centre of the phalanx (figure 1a,c,d,f). The furthest extent of resorption caused by the medullary cavity formation is marked by a resorption line, seen optically as a dark line surrounding the cavity (figure 1a,c; outlined in black) and as a bright white region (elevated concentration) in the map of iron (figure 1d,f; outlined in red). Between the lining of lamellar bone and the cavity void is a ring of compact cancellous bone of irregular thickness, which represents endosteal pathological bone deposition (figure 1a,c,d,f).

Elemental maps of iron (figures 1d–f and 2) and zinc (figure 2) show that chemistry is not uniformly distributed, but correlated with distinct bone tissue types, revealing histological details not observable via optical microscopy (histological thin section). Many of these details are affiliated with tissues seen in the calli and medullary cavity. Structures highlighted include laminar orientation of bone tissue located near the callus/normal bone interface in the medial section of the major callus (figure 1d indicated by a red arrow; figure 2b, respectively), the resorption line of the said cavity (figure 1c,f) and woven bone textures in pathological tissues (figures 1 and 2). The distribution of strontium and copper (the other elements known to strongly impact bone physiology) does not display differential uptake between tissue types.

Calcium concentrations are relatively uniform between bone tissue and the mineral infill, with concentrations comparable to those of fossil bone and calcite (figure 3b and table 1); however, phosphorus (figure 3a) is concentrated only within the fossil bone tissue. At the millimetre scale, zinc appears to be distributed evenly throughout the fossil bone (figure 3c); however, finer resolution scans of the pathological/normal bone interface reveal a strong distribution correlation between zinc and the woven pathological tissues of the main callus (figure 2).

Owing to the close proximity of the barium and lanthanum L-emission lines, these elements cannot be clearly windowed for the purposes of mapping, and therefore the

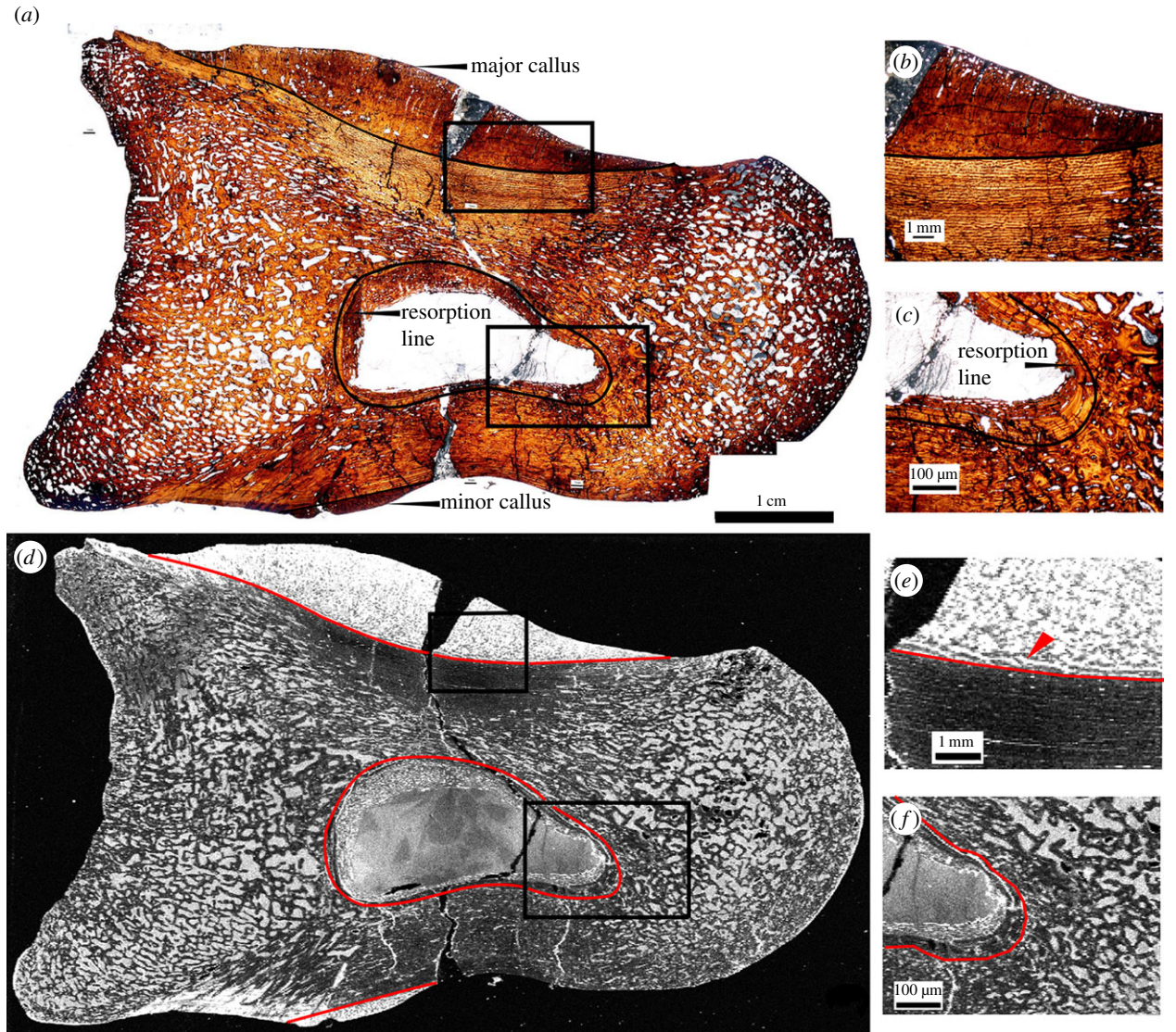


Figure 1. Thin section of *Allosaurus fragilis* (specimen UMNH 6282) pedal phalanx as seen in optical observation under plain polarized light (*a–c*) and in an elemental map of iron taken at the SSRL beamline 6-2 (*d–f*; grey scale relative image with white as high concentration, black as low). Calli are present on the dorsal (major callus) and ventral (minor callus) surfaces in both optical and elemental images. Photomicrographs (*b,c,e,f*) represent magnified views of areas of interests (boxed areas), including the major callus (*b,e*) and resorption cavity (*c,f*). Laminar orientation of bone tissue is observed in the map of iron around the interface of the major callus and normal cortical bone (*e*) that is not seen in thin section (*b*). The extent of resorption and woven bone infill of the medullary cavity are also enhanced in iron (*f*) compared with thin section (*c*).

map of lanthanum (figure 3*d*) inherently incorporates some signal from barium L-emission. However, processing the point analyses through PyMCA allowed for the identification and quantification of these two elements (electronic supplementary material). Lanthanum is concentrated mainly within the pathological tissue of the major dorsal callus with respect to all other bone tissues and the calcite infill of the fossil (figure 3*d*). All other areas of high concentration (bright spots) represent high concentrations of barium with respect to the entire thin section mount (table 1).

XAS of UMNH 6282 revealed sulfur speciation to be inorganic sulfate [46] (figure 4*a*), and zinc to be in a tetrahedral coordination with four oxygens within phosphate (figure 4*b* and the electronic supplementary material).

3.2. *Cathartes aura* (DMNH 83356)

Cancellous bone growths are observed under plane polarized light within the endosteal surface of the mid-shaft and on the distal articular surface (figure 5*a*). Pathological bone consists

of very poorly remodelled woven cancellous bone radiating from the original bone outline (figure 5*a*, pathological/normal bone interface marked in red). Pathological tissue was identified optically by the woven texture observed as the specimen is rotated in cross-polarized light. Elemental maps of calcium (figure 5*b*), phosphorus (figure 5*c*) and zinc (figure 5*d*) provide clear distinctions between the normal bone contour and the pathological bone growth, which is difficult to discern under optical observation, especially along the endosteal surface. Zinc and calcium concentrations are comparable to those found in other modern archosaurs [6] (table 2). Lanthanum is below the detection limit within the bone tissue (figure 5*e*), as expected for modern samples [7].

4. Discussion

The ability to distinguish fine details in the interpretation of pathological bone tissue is essential for physiological

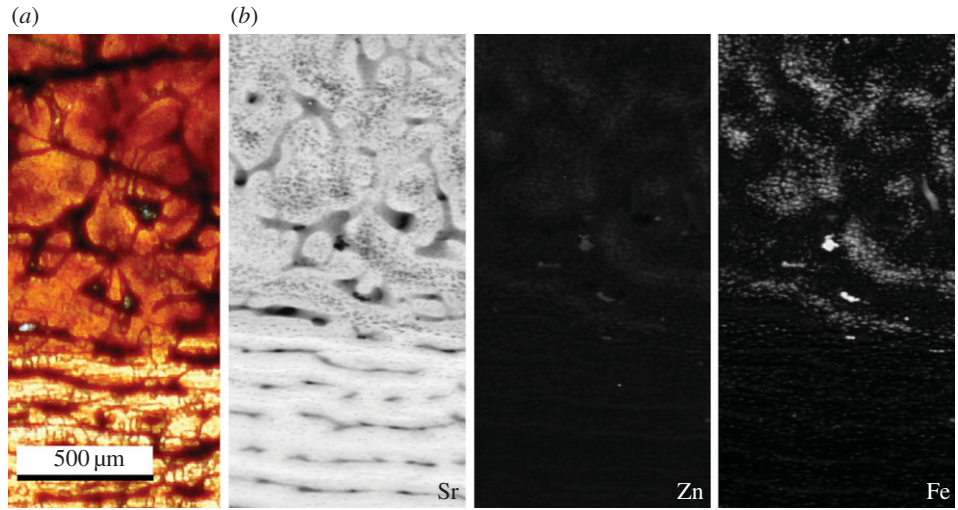


Figure 2. (a) Histological section as observed under plane polarized light and (b) false colour elemental maps of strontium, zinc and iron at the boundary between normal and pathological bone of the major callus in specimen UMNH 6282. The map of strontium highlights the woven texture of the callus, boundary of the bone tissues and laminar orientation of the normal bone. Zinc and iron are found mainly within the woven bone tissue of the callus.

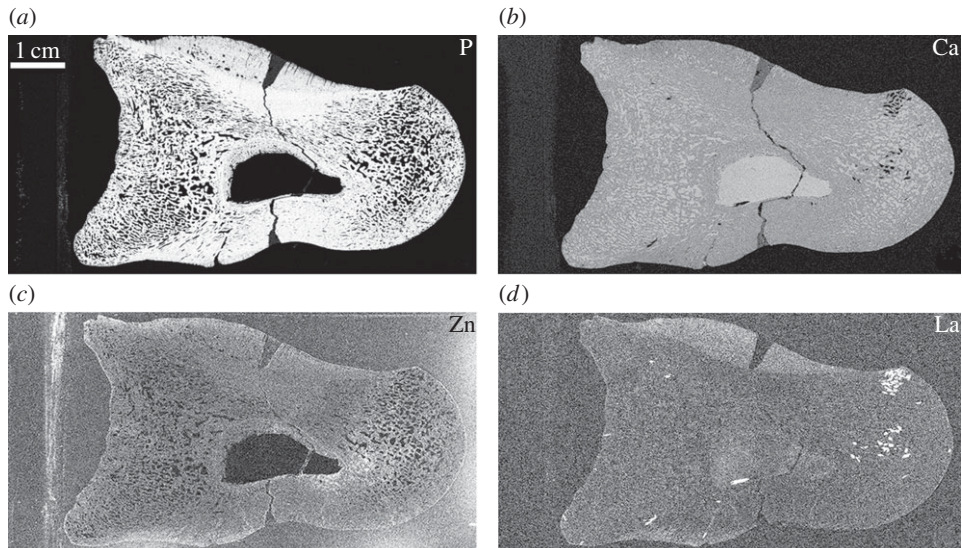


Figure 3. Elemental maps of phosphorus (a), calcium (b), zinc (c) and lanthanum (d) in UMNH 6282 taken at the SSRL beamline 6-2. Phosphorus is concentrated within the original tissue (a), whereas calcium concentrations are uniform throughout the entire specimen excluding the glass mounting slide of UMNH 6282 (b). Lanthanum is enriched in the pathological tissues of the calli (d). Owing to spectral overlap, the map of lanthanum convolves both lanthanum and barium. Lanthanum was distinguished from barium using PyMCA analysis [44].

interpretations of vertebrates. Optical histological analysis of fossilized tissues is strongly dependent on the quality of preservation of microstructures, which may be lost even within well-preserved fossils exhibiting exceptional gross morphology. In this study, large-scale high-resolution elemental mapping proved to be an effective tool in the interpretation of pathological healing strategies and histories within fossils where taphonomic processes may obscure fine histological features. Furthermore, elemental mapping proves to be a more powerful tool for discerning fine tissue features in extant material that may be obscured owing to sample preparation or size.

In *A. fragilis*, the discernibility of the morphological features from the pathological tissue of the major callus and endosteal bone growth within the medullary cavity was enhanced when compared with optical thin section observations. This includes details of the woven bone texture within the pathological tissue, as well as enhancement of the resorption line of the medullary cavity, which indicates

the farthest extension of bone resorption. The laminar orientation of bone tissue observed in iron between the main callus and normal cortical bone indicates the areas of resorption and remodelling of the callus not seen in optical observation [14].

In *C. aura*, elemental maps of calcium, phosphorus and zinc highlight the interface between normal and pathological tissues by providing a more accurate means to distinguish between pathological bone growth and the normal bone tissue outline, especially at the distal pathological/normal interface along the endosteal surface (figure 5). Elemental mapping thus provides additional morphological data compared with traditional optical thin section analysis, thereby allowing for the identification of discrete morphological features in both extant and extinct specimens.

Elemental maps revealed discrete elemental inventories unique to specific biological pathways within distinct tissue types, particularly in zinc. Zinc is usually correlated within areas of ossification, especially within areas of osteoid

Table 1. XRF point analysis concentrations taken at the SSRL of different bone tissue types and mounting slide of UMMNH 6282 and the Durango standard. Concentrations are given in ppm or weight per cent (wt%). The margin of error is approximately 10% of the absolute value. This is a conservative error value.

	epoxy/glass	Durango standard	major callus (dorsal)	callus/cortical edge	cortical bone	medullary cavity	minor callus (ventral)	possible HREE
high Z								
Ca	1.68 (wt%)	38.2 (wt%)	32.89 (wt%)	34.06 (wt%)	37.50 (wt%)	31.61 (wt%)	30.35 (wt%)	14.20 (wt%)
Mn	289	—	5587	2195	965	4270	4861	525
Fe	428	583.4	2.11 (wt%)	8620	2190	1.30 (wt%)	2.12 (wt%)	2127
Cu	4	—	18	30	20	11	25	12
Zn	45	32.26	69	57	62	62	118	41
Ba	469	0	0	117	0	0	696	28.25 (wt%)
La	0	5094	1107	1059	630	1079	749	0
Ce	0	7852	2611	3041	2629	914	2402	1466
low Z								
Si	4907	1021	1.27 (wt%)	—	2292	1.34 (wt%)	1.67 (wt%)	6734
P	856	18.17	17.99 (wt%)	—	32.97 (wt%)	14.35 (wt%)	29.32 (wt%)	16.11 (wt%)
S	1935	0	1.28 (wt%)	—	2.23 (wt%)	1.16 (wt%)	1.78 (wt%)	9.93 (wt%)

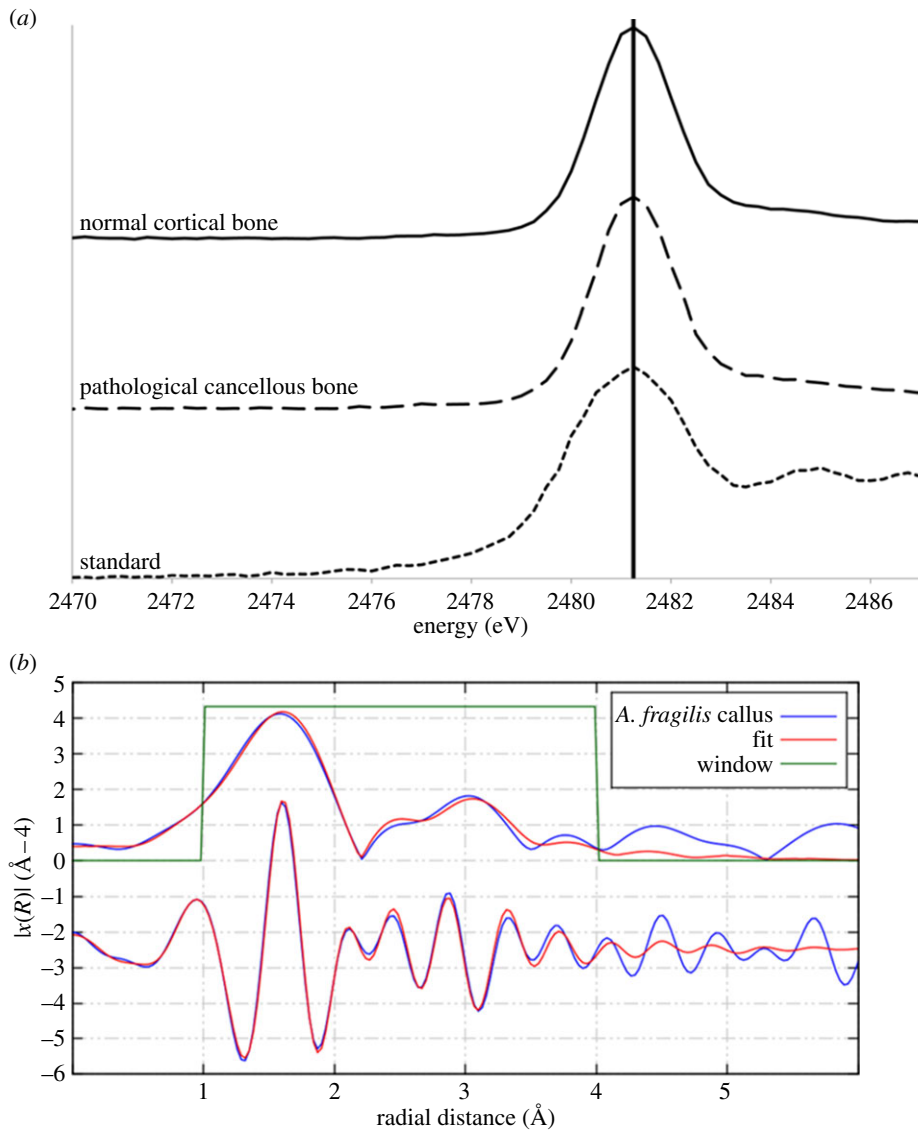


Figure 4. (a) XANES spectra for normal cortical bone taken from the dorsal surface and pathological bone taken from the main callus of UMNH 6282 compared with a sulfate standard. The peak for the sulfur species sulfate is marked [45]. (b) EXAFS spectrum for zinc taken from the main callus of UMNH 6282 revealing a tetrahedral coordination with phosphate.

mineralization such as within osteons [31,32,36,37]. The distribution of zinc was constrained within the woven tissue of the fracture callus in *A. fragilis*, a tissue type expected to be undergoing active ossification at time of death (figure 2). Quantification of zinc is slightly depleted (57–69 ppm) compared with modern archosaurs (100–250 ppm) [6,47] with the exception of the minor callus (118 ppm). This may suggest that at least a small portion of the original zinc has been removed by geological processes. If zinc has been removed from the fossil over time, then we should see the lowest concentrations of zinc in the more porous bone tissue (such as the calli and resorption cavity) and the outer edges of the bone as observed with the rare earth element (REE) concentrations (lanthanum). However, zinc concentrations remain fairly uniform throughout the entire specimen.

Conversely, the addition of zinc through pore water should also be taken into consideration, especially given the close association between the distribution of zinc and iron within the fracture callus as seen in figure 2. However, if zinc was introduced to the system, then we should see much higher concentrations than what is to be expected from modern bone (over 200 ppm). This trend is seen in

iron and lanthanum concentration profiles, suggesting an exogenous source to these elements. In addition, zinc EXAFS indicates that zinc is bound to four oxygen atoms in a tetrahedral coordination within phosphate, which is the coordination observed in hydroxyapatite [48]. If zinc had been added exogenously, then we would expect it to be coordinated with either the inorganic sulfate or an iron oxide. The zinc occupies the same positions as iron within the pathological bone tissue, but is not bound to the iron, suggesting that the zinc is endogenous.

In *C. aura*, zinc concentrations are elevated in the normal cortical tissue compared with the pathological cancellous tissue (table 2). Because we did not have access to this specimen at the microfocus beamline at DLS, we cannot say whether this discrepancy in concentrations is due to the large size of the pinhole at SSRL (50–100 µm), which is too large to distinguish between some of the finer histological features (i.e. cancellous struts). However, the concentrations of trace elements within *C. aura* calculated within this study are comparable with both other modern archosaurs and the *A. fragilis* specimen for exogenous elements such as calcium and zinc [6] (tables 1 and 2). We therefore

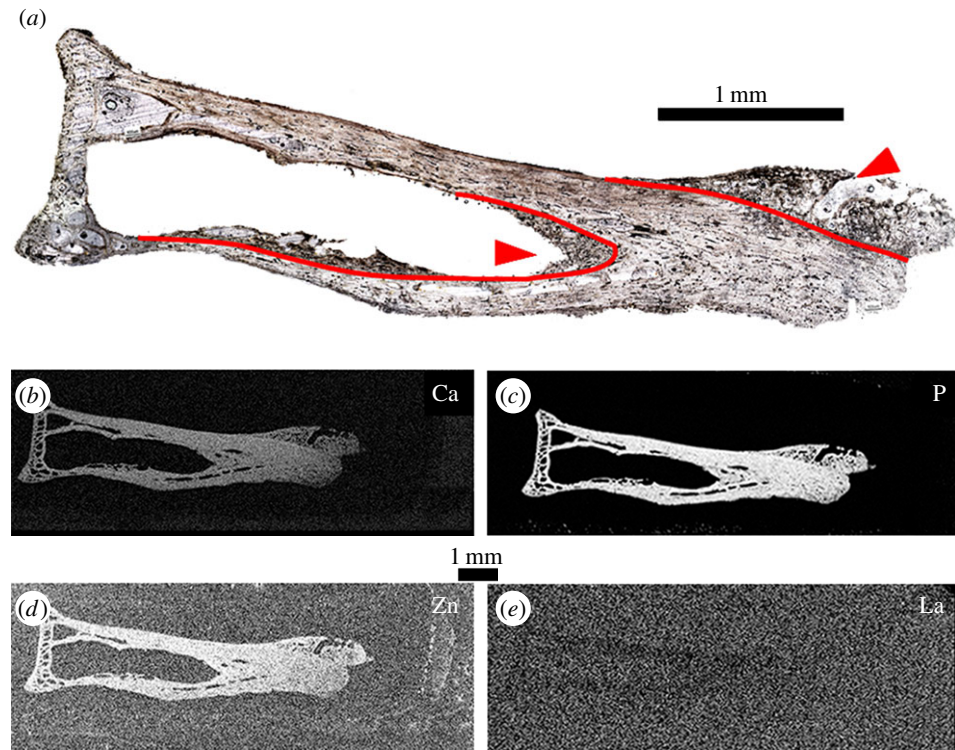


Figure 5. Thin section of DMNH 83356 as seen in optical observation under plane polarized light (*a*), calcium (*b*), phosphorus (*c*), zinc (*d*) and lanthanum (*e*) taken at SSRL (beamline 6-2). Woven pathological bone growth is present along both the endosteal surface of the mid-shaft and the distal articulation surface (arrowheads). The interface between pathological growth and the normal bone tissue outline is more distinct in elemental maps compared with optical observation (outlined in red), especially in determining the extent of pathological growth along the endosteal surface (*b–d*). Lanthanum is below detection limit within the bone tissue, which is expected in modern samples (*e*).

Table 2. High atomic weight element concentrations (Ca and heavier) in bone tissues and mounting slide of DMNH 83356 and the Durango standard. Concentrations are given in ppm or weight per cent (wt%). Error for heavy elements is approximately 10% of the absolute value. This is a conservative error value.

	epoxy/glass	Durango standard	pathological cancellous	normal cortical
Ca	1.72 (wt%)	38.2 (wt%)	30.64 (wt%)	25.86 (wt%)
Fe	392	583.4	212	167
Cu	2.44	—	11.20	40.30
Zn	43.30	32.26	198.47	221.13
As	0.37 (wt%)	870	0.27 (wt%)	0.21 (wt%)

suggest that zinc should be pursued as a possible biomarker for active ossification, and will be the subject of future work on both extant and extinct taxa. We were unable to discern differential uptake of strontium or copper between bone tissue types. Although copper concentrations appear to be slightly elevated within some tissue types, the difference in concentration is within the error of our quantification calculations.

Elemental mapping was also useful for determining the taphonomic history of a specimen through the diffusion patterns of elements as well as the quantification of elemental concentrations. The pattern and rate of elemental incorporation affects the rate of fossilization, which affects the probability of preserved original material through the degree of diagenetic alteration [9–12]. In *A. fragilis*, REE concentrations appear to follow simple diffusion patterns seen in most taphonomic studies where concentrations of REE decrease moving medially into the bone [7,10,12,49].

However, differences are observed between the pathological bone of the calli and the cancellous bone of the articular surfaces with concentrations of the light REE (lanthanum) elevated within the pathological tissue compared with all normal bone tissues. Because the common factors that affect REE uptake are similar for both tissue types (bone porosity, location to surface of the bone, size of element), another tissue property must be responsible. One possibility is that the calli were still soft (cartilage present) at least at the outer surface of the callus. Soft tissues would degrade quickly, exposing the porous pathological bone faster than the normal cancellous bone, which is surrounded by the dense lamellar bone of the outer circumferential layer. If this callus is the result of fracture healing, then the presence of cartilage in a callus that histologically appears to be very well remodelled would indicate a more reptilian style of callus, which is more cartilaginous than mammalian calli in later stages of remodelling [28–30].

The identification of cartilage is important for a number of biological interpretations, including maturity (age), size (length and height), biomechanics and healing strategies. Currently, identification of cartilage in the fossil record is based on morphological data [1], and a definitive trace metal biomarker for cartilage is yet to be identified. Morphological indicators of cartilage include attachment features such as the ‘pitted’ appearance of the articular ends of podial elements and the histological identification of calcified cartilage [1]. Unfortunately, fracture callus cartilage does not leave such morphological evidence on the surrounding bone. Therefore, future work on the effects of cartilage on REE uptake in modern and fossil bone is needed to test whether REE profiling may be helpful in the identification and quantification of cartilage in extinct organisms.

In the case of UMNH 6282, calcium concentrations are constant throughout the specimen, which suggests calcium remains immobile through the fossilization environment (table 1). This is not surprising as the lithologies of the Cleveland-Lloyd Dinosaur Quarry are highly calcareous, which would account for the calcite infill of the bone [50,51] and the stability of endogenous bone calcium. Concentrations of iron are elevated compared with modern bone (wt% versus ppm) [6], suggesting an exogenous source (table 1). Sulfur was found to be present as inorganic sulfate rather than organic sulfur, suggesting that any original sulfur has been lost diagenetically. The incorporation of elemental data of the surrounding matrix would aid in determining the origin of the sulfur; however, this specimen had already been prepared before analysis. Furthermore, the heterogeneous nature of the site makes it difficult to collect a matrix sample for future analysis, because the sample may not be representative of the area from which the specimen was collected [50,51].

5. Conclusion

SRS-XRF elemental mapping provides a de novo approach to distinguish fine bone tissue chemistry and morphologies of extant and extinct specimens not observed in conventional histological thin section analysis. Many of these features occur at the boundaries between different tissue types, such as between pathological and normal bone, leading to more developed interpretations of healing strategies within archosaurs. Elemental maps also reveal a selective distribution of zinc within areas of possible active ossification in the pathological callus tissue of *A. fragilis*, suggesting a possible trace metal biomarker for the ossification process. This marks the first instance of a possible trace element biomarker for a biosynthetic pathway within fossilized bone tissue.

Future studies employing chemical analysis (SRS-XRF, Fourier transform infrared spectroscopy, etc.) are needed to resolve the identification and interpretation of trace metal biomarkers crucial to bone physiology. Coupled with the application of micro-computed tomography structural analysis, this approach could lead to the identification of bone healing strategies (callus architecture, protein pathways, speed of healing, etc.) used among extinct vertebrates.

Acknowledgements. We thank Dr Randy Irmis at the Natural History Museum of Utah and Dr Jean Woods at the Delaware Museum of Natural History for supplying specimens for analysis, Dr Dennis Terry, Jr and Dr David Grandstaff at Temple University for their insights, the staff of the Stanford Synchrotron Radiation Lightsource, SLAC National Accelerator Laboratory and Diamond Light Source for their splendid support in aiding our team with the synchrotron-based analyses, NERC and STFC for their funding of our synchrotron work, and the University of Manchester Dean’s Fund (awarded to J.A.) for their financial support for our PhD students. We also thank the three reviewers who made helpful comments that strengthened our manuscript. The authors also acknowledge the support of the Interdisciplinary Centre for Ancient Life (University of Manchester).

References

- Chinsamy-Turan A. 2005 *The microstructure of dinosaur bone: deciphering biology with fine-scale techniques*. Baltimore, MD: The John Hopkins University Press.
- Currey J. 2002 *Bones: structure and biomechanics*. Princeton, NJ: Princeton University Press.
- de Ricqlés A. 1974 Evolution of endothermy: histological evidence. *Evol. Theor.* **1**, 51–80.
- Tumarkin-Deratzian AR, Vann DV, Dodson P. 2006 Bone surface texture as an ontogenetic indicator in long bones of the Canada goose *Branta Canadensis* (Anseriformes: Anatidae). *Zool. J. Linn. Soc. Lond.* **148**, 133–168. (doi:10.1111/j.1096-3642.2006.00232.x)
- Madsen J. 1976 *Allosaurus fragilis*: a revised osteology. *Utah Geol. Surv. Bull.* **109**, 1–163.
- Goodwin MB, Grant PG, Bench G, Holyrod P. 2007 Elemental composition and diagenetic alteration of dinosaur bone: distinguishing micron-scale spatial and compositional heterogeneity using PIXE. *Palaeogeogr. Palaeoclimatol. Palaeoecol.* **23**, 458–476. (doi:10.1016/j.palaeo.2007.06.017)
- Trueman CN, Tuross N. 2002 Trace elements in recent and fossil bone apatite. *Rev. Mineral. Geochem.* **48**, 489–521. (doi:10.2138/rmg.2002.48.13)
- Wopenka B, Pasteris J. 2005 A mineralogical perspective on the apatite in bone. *Mater. Sci. Eng. C* **25**, 131–143. (doi:10.1016/j.msec.2005.01.008)
- Fricke HC, Rogers RR. 2000 Multiple taxon – multiple locality approach to providing oxygen isotope evidence for warm-blooded theropod dinosaurs. *Geology* **28**, 799–802. (doi:10.1130/0091-7613(2000)28<799:MTLATP>2.0.CO;2)
- Herwartz D, Tütken T, Jochum KP, Sander PM. 2012 Rare earth element systematics of fossil bone revealed by LA-ICPMS analysis. *Geochim. Cosmochim. Acta* **103**, 161–183. (doi:10.1016/j.gca.2012.10.038)
- Kocsis L, Trueman CN, Palmer MR. 2010 Protracted diagenetic alteration of REE contents in fossil bioapatites: direct evidence for Lu-Hf isotope systematics. *Geochim. Cosmochim. Acta* **74**, 6077–6092. (doi:10.1016/j.gca.2010.08.007)
- Kohn MJ, Moses RJ. 2013 Trace element diffusivities in bone rule out simple diffusive uptake during fossilization but explain *in vivo* uptake and release. *Proc. Natl Acad. Sci. USA* **10**, 419–422. (doi:10.1073/pnas.1209513110)
- Kohn M. 2008 Models of diffusion-limited uptake of trace elements in fossils and rates of fossilization. *Geochim. Cosmochim. Acta* **72**, 3758–3770. (doi:10.1016/j.gca.2008.05.045)
- Edwards NP, Barden H, van Dongen BE, Manning PL, Larson P, Bergmann U, Sellers WI, Wogelius RA. 2011 Infra-red mapping resolves soft-tissue preservation in 50 million year old reptile skin. *Proc. R. Soc. B* **278**, 3209–3218. (doi:10.1098/rspb.2011.0135)
- Stankiewicz BA, Briggs DEG, Evershed RP, Flannery MB, Wuttke M. 1997 Preservation of chitin in 25-million-year-old fossils. *Science* **276**, 1541–1543. (doi:10.1126/science.276.5318.1541)
- Vitek NS, Vinther J, Schiffbauer JD, Briggs DEG, Prum RO. 2013 Exceptional three-dimensional preservation and coloration of an originally iridescent fossil feather from the middle Eocene messel oil shale. *Paläontol. Z.* **87**, 493–503. (doi:10.1007/s12542-013-0173-5)
- Bergmann U, Morton RW, Manning PL, Sellers WI, Farrar S, Huntley KG, Wogelius RA, Larson P. 2010 *Archaeopteryx* feathers and bone chemistry fully revealed via synchrotron imaging. *Proc. Natl Acad. Sci. USA* **107**, 9060–9065. (doi:10.1073/pnas.1001569107)

18. Bergmann U, Manning PL, Wogelius RA. 2012 Chemical mapping of paleontological and archaeological artefacts using synchrotron x-rays. *Ann. Rev. Anal. Chem.* **5**, 361–389. (doi:10.1146/annurev-anchem-062011-143019)
19. Wogelius RA et al. 2011 Trace metals as biomarkers for eumelanin pigment in the fossil record. *Science* **333**, 1622–1626. (doi:10.1126/science.1205748)
20. Edwards NP et al. 2014 Leaf metallome preserved over 50 million years. *Metalomics* **6**, 774–782. (doi:10.1039/C3MT00242J)
21. Straight W, Davis G, Skinner C, Haims A, McClellan B, Tanke D. 2009 Bone lesions in *Hadrosaurus*: computed tomographic imaging as a guide for paleohistological and stable-isotope analysis. *J. Vertebr. Paleontol.* **29**, 315–325. (doi:10.1671/039.029.0211)
22. Skinner HCW. 2005 Mineralogy of bone. In *Essentials of medical geology* (eds O Selinus et al.), pp. 667–693. Burlington, MA: Elsevier Academic Press.
23. Pasteris J, Wopenka B, Freeman J, Rogers K, Valsami-Jones E, van der Houwen J, Silva M. 2004 Lack of OH in nanocrystalline apatite as a function of degree of atomic order: implications for bone and biomaterials. *Biomaterials* **25**, 229–238. (doi:10.1016/S0142-9612(03)00487-3)
24. Carter D, Beaupré G. 2001 *Skeletal function and form: mechanobiology of skeletal development, aging, and regeneration*. New York, NY: Cambridge University Press.
25. Waldron T. 2009 *Paleopathology*. New York, NY: Cambridge University Press.
26. Ferguson C, Alpern E, Midau T, Helms J. 1999 Does fracture repair recapitulate embryonic skeletal formation? *Mech. Dev.* **87**, 57–66. (doi:10.1016/S0925-4773(99)00142-2)
27. Shapiro F. 2008 Bone development and its relation to fracture repair. The role of mesenchymal osteoblasts and surface osteoblasts. *Eur. Cells Mater.* **15**, 53–76.
28. Pritchard JJ, Ruzicka AJ. 1950 Comparison of fracture repair in the frog, lizard, and rat. *J. Anat.* **84**, 236–261.
29. Raftery A. 2011 Reptile orthopaedic medicine and surgery. *J. Exot. Pet Med.* **20**, 107–116. (doi:10.1053/j.jepm.2011.02.005)
30. Beatty B, Rothschild B. 2009 Paleopathologies are features of an organism and its interaction with the environment and should not be treated like organisms unto themselves. *Hist. Biol.* **21**, 229–233. (doi:10.1080/08912960903469711)
31. Barbara A, Delannoy P, Denis BG, Marie PG. 2004 Normal matrix mineralization induced by strontium renelate in MC3T3-E1 osteogenic cells. *Metabolism* **53**, 532–537. (doi:10.1016/j.metabol.2003.10.022)
32. Bonnelye E, Chabadel A, Salte F, Jurdic P. 2008 Dual effect of strontium ranelate: stimulation of osteoblast differentiation and inhibition of osteoclast formation and resorption *in vitro*. *Bone* **42**, 129–138. (doi:10.1016/j.bone.2007.08.043)
33. Yuan X, Wang J, Zhu X, Zhang Z, Ai Y, Sun G, Wang Z, Liu G. 2011 Effect of copper on levels of collagen and alkaline phosphatase activity from chondrocytes in newborn piglets *in vitro*. *Biol. Trace Elem. Res.* **144**, 597–605. (doi:10.1007/s12011-011-9151-5)
34. Yamaguchi M. 2010 Role of nutritional zinc in the prevention of osteoporosis. *Mol. Cell. Biochem.* **338**, 241–254. (doi:10.1007/s11010-009-0358-0)
35. Lowe NM, Fraser WD, Jackson MJ. 2002 Is there a potential therapeutic value of copper and zinc for osteoporosis? *Proc. Nutr. Soc.* **61**, 181–185. (doi:10.1079/PNS2002154)
36. Gomez S, Rizzo R, Pozzi-Mucelli M, Bonucci E, Vittur F. 1999 Zinc mapping in bone tissues by histochemistry and synchrotron radiation-induced X-ray emission: correlation with the distribution of alkaline phosphates. *Bone* **25**, 33–38. (doi:10.1016/S8756-3282(99)00102-7)
37. Haumont S. 1961 Distribution of zinc in bone tissue. *J. Histochem. Cytochem.* **9**, 141–145. (doi:10.1177/9.2.141)
38. Rucker RB, Kononen T, Clegg MS, Mitchell AE, Rucker BR, Uriu-Hare JY, Keen CL. 1998 Copper, lysyl oxidase, and extracellular matrix protein cross-linking. *Am. J. Clin. Nutr.* **67**(Suppl.), 996S–1002S.
39. Brown Jr GE, Strurchio NC. 2002 An overview of synchrotron radiation applications to low temperature geochemistry and environmental science. *Rev. Mineral. Geochem.* **49**, 1–115. (doi:10.2138/gsrmg.49.1.1)
40. Morton RW, Witherspoon KC. 1993 Elemental X-ray imaging of fossils. *Adv. X-Ray Anal.* **36**, 97–104.
41. Chinsamy A, Raath MA. 1992 Preparation of fossil bone for histological examination. *Paleontol. Afr.* **29**, 39–44.
42. Abramoff MD, Magelhaes PJ, Ram SJ. 2004 Image processing with IMAGE. *Biophotonics Int.* **11**, 36–42.
43. Chinga G, Syverud K. 2007 Quantification of paper mass distributions within local picking areas. *Nord. Pulp Pap. Res. J.* **22**, 441–446. (doi:10.3183/NPPRJ-2007-22-04-p441-446)
44. Solé VA, Papillon E, Cotte M, Walter Ph, Susini J. 2007 A multiplatform code for the analysis of energy-dispersive X-ray fluorescence spectra. *Spectrochim. Acta B* **62**, 63–68. (doi:10.1016/j.sab.2006.12.002)
45. Ravel B, Newville M. 2005 *Athena, Artemis, Hephaestus*: data analysis for x-ray absorption spectroscopy using IFEFFIT. *J. Synchrotron Radiat.* **12**, 537–541. (doi:10.1107/S0909049505012719)
46. Sandström M, Jalilehvand F, Damain E, Fors Y, Gelius U, Jones M, Salomé M. 2005 Sulphur accumulation in the timbers of King Henry VIII's warship *Mary Rose*: a pathway in the sulphur cycle of conservation concern. *Proc. Natl. Acad. Sci. USA* **102**, 14 165–14 170. (doi:10.1073/pnas.0504490102)
47. Parslow JLF, Jefferies DJ, French MC. 1972 Ingested pollutants in puffins and their eggs. *Bird Study* **19**, 18–33. (doi:10.1080/00063657209476321)
48. Tang Y, Chappell HF, Dove MT, Reeder RJ, Lee YJ. 2009 Zinc incorporation into hydroxylapatite. *Biomaterials* **30**, 2864–2872. (doi:10.1016/j.biomaterials.2009.01.043)
49. Suarez C, Macpherson G, González L, Grandstaff G. 2010 Heterogeneous rare earth element (REE) patterns and concentrations in a fossil bone: implications for the use of REE in vertebrate taphonomy and fossilization history. *Geochim. Cosmochim. Acta* **74**, 2970–2988. (doi:10.1016/j.gca.2010.02.023)
50. Bilbey S. 1998 Cleveland–Lloyd dinosaur quarry: age, stratigraphy, and depositional environments. *Mod. Geol.* **22**, 87–120.
51. Gates T. 2005 The late Jurassic Cleveland–Lloyd dinosaur quarry as a drought-induced assemblage. *Palaios* **20**, 363–375. (doi:10.2110/palo.2003.p03-22)

Synchrotron imaging reveals bone healing and remodeling strategies in extinct and extant vertebrates

Jennifer Anné¹, Nicholas P. Edwards¹, Roy A. Wogelius*¹, Allison R. Tumarkin-Deratzian², William I. Sellers³, Arjen van Veelen¹, Uwe Bergmann⁴, Dimosthenis Sokaras⁵, Roberto Alonso-Mori⁵, Konstantin Ignatyev⁶, Victoria M. Egerton¹, Phillip, L. Manning*¹

¹University of Manchester, School of Earth, Atmospheric and Environmental Science, Williamson Research Centre for Molecular Environmental Science, Manchester M13 9PL, UK

²Department of Earth and Environmental Science, Temple University, Philadelphia, PA, 19122, USA

³University of Manchester, Faculty of Life Sciences, Manchester M13 9PL, UK

⁴SLAC National Accelerator Laboratory, Linac Coherent Light Source, Menlo Park, CA, 94025, USA

⁵SLAC National Accelerator Laboratory, Stanford Synchrotron Radiation Lightsource, Menlo Park, CA 94025, USA

⁶Diamond Light Source, Didcot, OX11 0DE, UK

*corresponding authors: phil.manning@manchester.ac.uk; roy.wogelius@manchester.ac.uk

SUPPLEMENTARY MATERIAL

1. Fossil Locality Descriptions

1.1 Cleveland-Lloyd Dinosaur Quarry (CLDQ)

The CLDQ is located in Emery County, Utah, USA within the lower Brushy Basin Member, the most laterally-extensive unit in the Morrison Formation (Late Jurassic, Kimmeridgian to Tithonian; 153-145 ma)[1-3]. It consists of silty mudstone with an overlying, fossiliferous calcareous mudstone capped by a freshwater limestone, which is in turn overlain by a volcanic ash bed [1-2]. The main bone-bearing unit at the CLDQ is a massive, smectitic mudstone consisting mainly of montmorillonite, but also containing large amounts of quartz, feldspar, biotite, and clasts of volcanic and sedimentary rock [1-2]. Diagenetic limestone nodules are common. Based on the presence of charophytes and ostracodes, along with a lack of rhizoliths and evidence of soil oxidation, this unit is interpreted as a seasonally wet environment [1-2].

The majority of the vertebrates found at the CLDQ are dinosaurian with 66% of the fauna represented by the theropod *Allosaurus fragilis* (about 44-46 individuals) [2-3]. Of those 46 individuals, 82% are identified as juvenile or sub-adult in age. The unusually high predator/prey ratio found at this site (about 3:1) has led to the hypothesis that this was a natural predator trap [1, 3]. However, an unusually

high number of juveniles coupled with an assemblage of freshwater invertebrate fossils suggest a seasonal lake, which would have been a ready source of water unless there was a drought [2].

2. Specimen Handling and Preparation

One of the concerns with elemental mapping is the use of glues and other preservation polymers. Most conventional museum conservation techniques include the use of various adhesives and stabilisers to prevent the loss of fossil material due to handling and storage. Although these polymers aid in the preservation of visible features, they can be extremely damaging to the original chemistry of the specimen. Damage and contamination due to handling are limited to after the specimen was thin sectioned as the section represents internal tissues not exposed during museum storage. However, adhesives were used in the construction of thin sections.

In this study, Paleobond® penetrant stabiliser was used to prevent specimens from flaking during polishing. The chemical composition of Paleobond® is listed as 95-100% Ethyl Cyanoacrylate ($C_6H_7NO_2$), with a 0-0.5% Hydroquinone ($C_6H_6O_2$) possible. For mounting specimens to glass slides, we use a two part Hillquist thin section epoxy (Part A and B), which include a mixture of epoxy and polyamide resin. Point analysis of the mounting epoxy was taken for each thin section slide at both high and low-Z to determine the trace element composition of the adhesive (tables 1 and 2).

3. Location of Point Analyses

To quantify the concentrations of elements within a sample, point analyses were selected by; locating an area of interest within the scan, driving the stage to the point coordinates, and collecting a full energy spectrum for 50 seconds. Three point analyses for high-Z (Ca and heavier) and two for low-Z (Ca and lighter) scans were taken at each area of interest and averaged to account for sample heterogeneity (figures S1 and S2).

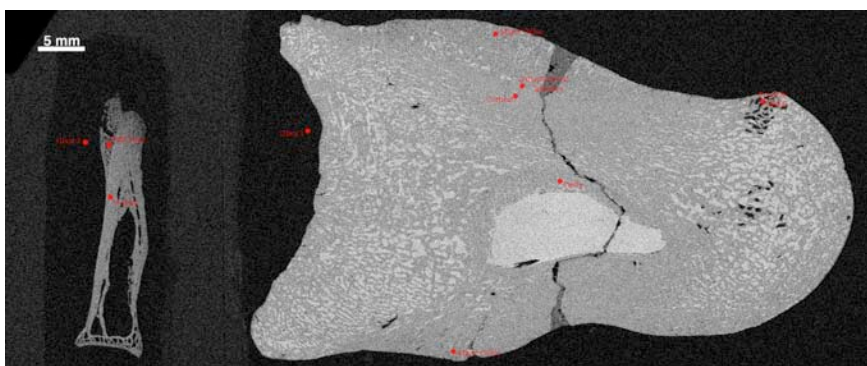


Figure S1: Location of point analysis (red dots) taken at high-Z. Points are overlaid on the map of Ca. The size of the dot is not proportional to the size of the beam area on the specimen, but has been enlarged for visibility. Labels represent the concentrations seen in tables 1 and 2 in the main text.

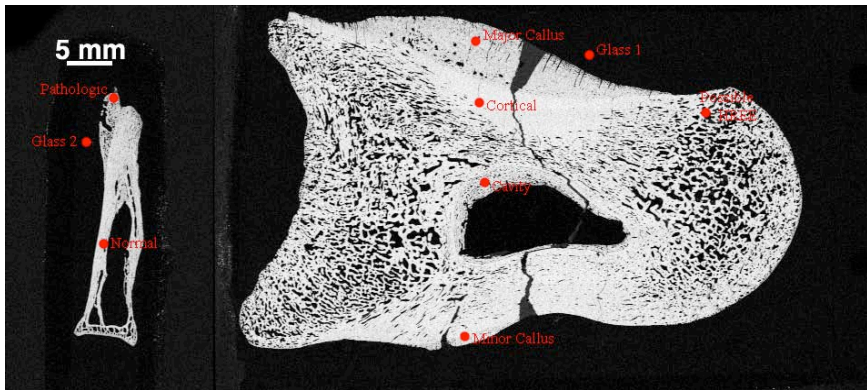


Figure S2: Location of point analysis (red dots) taken at low-Z. Points are overlaid on the map of P. The size of the dot is not proportional to the size of the beam area on the specimen, but has been enlarged for visibility. Labels represent the concentrations seen in tables 1 and 2 in the main text.

4. Quantification Using PyMca

Full EDS spectra obtained at both beamlines are fit using PyMCA freeware [4] by incorporating fundamental parameters of the experiment and a Durango apatite mineral standard with known element concentrations for calibration (see example EDS files).

We do realise that absolute concentrations obtained with this method should be treated with caution due to the many geometric factors involved. However, the 10% absolute value error we place on these quantifications is a conservative one.

In addition, calculated concentrations for the Durango apatite mineral standard using synchrotron XRF are comparable with those obtained on the same sample using microprobe analysis. This includes 1) Ca: 38.2 wt% PyMca, 38.19 wt% microprobe; 2) Fe: 583 ppm PyMca, range between 248-404 ppm microprobe; 3) La: 5094 ppm PyMca, 4290 ppm microprobe; and 4) Ce: 7852 ppm PyMca, 5868 ppm microprobe. All concentrations, peak fit statistics, and fitting errors are included in the EDS spectrum within the supplementary material. The accuracy and precision of SRS-XRF point analyses, once calibrated using mineral standards, is thus shown to be fully quantitative, as long as the errors on the concentrations are clearly stated.

Lastly, quantification is obtained primarily to confirm that the elements of interest are in concentrations comparable to those found in living tissues rather than extremely elevated or depleted concentrations expected with inorganic geological precipitation or leaching.

5. Extended X-Ray Absorption Fine Structure (EXAFS)

EXAFS fitting was done through the use of the Demeter software package [5]. Several coordination's were considered for the fit, including zinc phosphate, zincite, zinc carbonate, Zn-Fe oxides, and zinc

sulphate. Below is the log results from our fit of the zinc EXAFS taken from the major callus of UMNH 6282, which revealed the zinc to be a zinc phosphate.

```
Name          : Fit 31      (qksnk)
Description   : fit to i18-22464.dat
Figure of merit : 31
Time of fit    : 2014-03-06T09:19:19
Environment    : Demeter 0.9.19 with perl 5.018001 and using Iffeffit 1.2.12 on
Windows 8
Interface     : Artemis (Wx 0.9922)
Prepared by   :
Contact       :

=====
Independent points      : 12.5976563
Number of variables     : 6
Chi-square              : 3.3061091
Reduced chi-square       : 0.5011036
R-factor                 : 0.0091054
Measurement uncertainty (k) : 0.0138706
Measurement uncertainty (R) : 0.0159073
Number of data sets      : 1

Happiness = 100.00/100           color = #D8E796
***** Note: happiness is a semantic parameter and should *****
***** NEVER be reported in a publication -- NEVER! *****

guess parameters:
amp                  = 0.92796118    # +/- 0.03633686      [0.96869]

set parameters:
enot                = -0.73650000
NO                  = 4.05864000
delr_O               = 0.03972000
ss_O                = 0.00883000
NZn                 = 2.12887000
delr_Zn              = 0.09000000
ss_Zn                = 0.00655000
NP                  = 1.10775000
delr_P               = -0.25955000
ss_P                = 0.01698000

Correlations between variables:
All other correlations below 0.4

===== Data set >> i18-22464.dat << =====

: Athena project      = C:\Users\AvV\Documents\Bibliotheek\13 - Palaeo-
work\EXAFSAlloToeZn\EXAFSAlloToeZn\AlloZnEXAFS_deglitch.prj, 1
: name                 = i18-22464.dat
: k-range              = 3.0 - 8.0559
: dk                   = 1
: k-window             = hanning
: k-weight              = 1,2,3
: R-range              = 1 - 4
: dR                   = 0.0
: R-window             = hanning
: fitting space        = r
: background function  = yes
: phase correction     =
```

```

: R-factor by k-weight = 1 -> 0.01003, 2 -> 0.00938, 3 -> 0.00939

      name          N        S02      sigma^2     e0      delr      Reff      R
=====
O1.1          1.000    3.766    0.00883   -0.737   0.03972   1.97800   2.01772
Zn1.1          1.000    1.976    0.00655   -0.737   0.09000   3.20900   3.29900
P2.2          1.000    1.028    0.01698   -0.737  -0.25955   3.07070   2.81115

      name          ei       third      fourth
=====
O1.1          0.00000   0.00000   0.00000
Zn1.1          0.00000   0.00000   0.00000
P2.2          0.00000   0.00000   0.00000

```

REFERENCES

1. Bilbey, S. 1998. Cleveland-Lloyd Dinosaur Quarry- Age, stratigraphy, and depositional environments. *Modern Geology* **22**, 87-120.
2. Gates, T. 2005. The Late Jurassic Cleveland-Lloyd Dinosaur Quarry as a drought-induced assemblage. *Palaios* **20**, 363-375.
3. Madsen, J. 1976, *Allosaurus fragilis*: A Revised Osteology; *Utah Geological Survey Bulletin* **109**.
4. Solé, V.A., Papillon, E., Cotte, M., Walter, Ph., & Susini, J. 2007. A multiplatform code for the analysis of energy-dispersive x-ray fluorescence spectra. *Spectrochim. Acta B* **62**, 63-68.
5. Ravel, B. & Newville, M. 2005. *Athena, Artemis, Hephaestus*: data analysis for x-ray absorption spectroscopy using IFEFFIT. *J. Synchrotron Rad.* **12**, 537-541.

PyMCA : Advanced Fit Results

| [PyMCA home](#) | [ESRF home](#) | [BLISS home](#) | [Concentrations](#) | [Fit Peak Results](#)



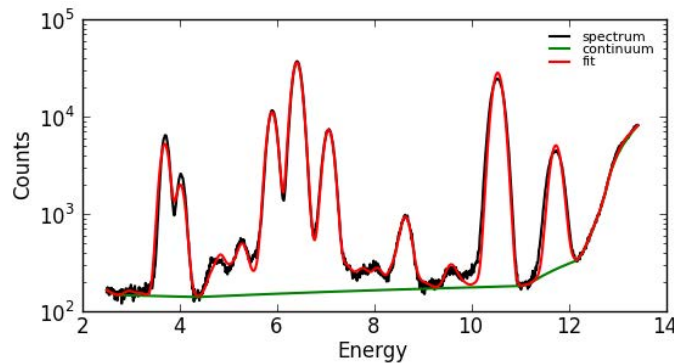
Computed File : C:/Users/mbexjja4/Documents/PhDResearch/Manuscripts/Interface/Revision1/M13_DINOBI

Source : [C:/Users/mbexjja4/Documents/PhDResearch/SSRL_Mar2013/Mar 2013 Final Package/M13_Spectra/M13_DINOBIRD_DINOGL_CAL1_HZ.mca]

Selection : M13_DINOBIRD_DINOGL_CAL1_HZ.mca 2.1.1.1

Parameters : [M13_DINOBIRD_DINOGL_CAL1_HZ.mca_2.1.1.1.txt](#)

Spectrum, Continuum and Fitted values :



Fit Parameters :

FIT parameters	
Region of Fit	250 - 1345
Number of iterations	2
Chi square	51.0419
Last Chi square difference	5507424.4227 %
Calibration parameters	
Zero	4.30438E-03 +/- 4.30438E-03
Gain	9.97000E-03 +/- 9.97000E-03
Noise	1.90000E-01 +/- 1.90000E-01
Fano	1.20000E-01 +/- 1.20000E-01
Sum	0.00000E+00 +/- 0.00000E+00
Continuum parameters	
Type	Strip Background
Strip Constant	1.00000
Strip Iterations	20000
Strip Width	4
Smoothing Filter Width	10

Concentrations:

Element	Group	Fit Area	Sigma Area	M	a s s f r a c t i o n	Layer0
P	K	0.000000e+00	0.00e+00	0	0	
Ar	K	5.589258e+02	8.88e+01	0.09845	0.09845	
Ca	K	1.582589e+05	4.13e+02	0.2955	0.2955	
Mn	K	3.189016e+05	7.62e+02	0.008823	0.008823	
Fe	K	1.011873e+06	1.14e+03	0.01468	0.01468	
Cu	K	2.200256e+03	2.31e+02	7.748e-06	7.748e-06	
Zn	K	2.122108e+04	2.45e+02	5.121e-05	5.121e-05	
As	K	8.944017e+05	9.58e+02	0.0009595	0.0009595	
Ba	L	0.000000e+00	0.00e+00	0	0	
La	L	8.303147e+03	2.58e+02	0.00161	0.00161	
Ce	L	1.965356e+04	2.93e+02	0.002533	0.002533	

PyMCA : Advanced Fit Results

Nd	L	0.000000e+00	0.00e+00	0	0
Eu	L	5.459378e+03	1.15e+03	0.0001339	0.0001339
Gd	L	1.365862e+04	5.06e+02	0.0002583	0.0002583
Dy	L	1.983017e+03	6.02e+02	2.268e-05	2.268e-05
Er	L	1.494687e+03	3.19e+02	1.092e-05	1.092e-05
Tm	L	5.971506e+02	4.83e+02	3.55e-06	3.55e-06
Yb	L	7.710416e+03	3.31e+02	3.819e-05	3.819e-05
Lu	L	3.434955e+03	3.23e+02	1.394e-05	1.394e-05
Hf	L	0.000000e+00	0.00e+00	0	0

Fit Peak Results:

Element	Group	Fit Area	Sigma	Energy	Ratio	FWHM	Chi square
P	K	0.000000e+00	0.00e+00				
	KL3	0.000000e+00	0.00e+00	2.010	0.42423	0.203	0.00
	KM3	0.000000e+00	0.00e+00	2.136	0.57577	0.204	0.00
Ar	K	5.589258e+02	8.88e+01				
	KL3	3.673340e+02	5.84e+01	2.957	0.65721	0.209	1.19
	KM3	1.915918e+02	3.04e+01	3.190	0.34279	0.210	3.37
Ca	K	1.582589e+05	4.13e+02				
	KL3	1.157131e+05	3.02e+02	3.691	0.73116	0.213	171.30
	KM3	4.254580e+04	1.11e+02	4.013	0.26884	0.215	58.57
Mn	K	3.189016e+05	7.62e+02				
	KL2	8.754600e+04	2.09e+02	5.888	0.27452	0.226	38.94
	KL3	1.735691e+05	4.15e+02	5.899	0.54427	0.226	43.01
	KM3	5.778658e+04	1.38e+02	6.490	0.18121	0.230	52.97
Fe	K	1.011873e+06	1.14e+03				
	KL2	2.807767e+05	3.16e+02	6.391	0.27748	0.229	76.27
	KL3	5.554115e+05	6.26e+02	6.404	0.54889	0.229	74.61
	KM3	1.756852e+05	1.98e+02	7.058	0.17362	0.233	11.31
Cu	K	2.200256e+03	2.31e+02				
	KL2	6.261488e+02	6.58e+01	8.028	0.28458	0.238	2.25
	KL3	1.230586e+03	1.29e+02	8.048	0.55929	0.238	2.26
	KM3	3.435210e+02	3.61e+01	8.905	0.15613	0.243	2.60
Zn	K	2.122108e+04	2.45e+02				
	KL2	6.064413e+03	7.01e+01	8.616	0.28577	0.241	1.85
	KL3	1.189861e+04	1.38e+02	8.639	0.56070	0.241	1.99
	KM3	3.258060e+03	3.77e+01	9.572	0.15353	0.246	2.78
As	K	8.944017e+05	9.58e+02				
	KL2	2.575074e+05	2.76e+02	10.508	0.28791	0.251	417.38
	KL3	5.027088e+05	5.38e+02	10.544	0.56206	0.251	402.80
	KM3	1.293439e+05	1.39e+02	11.724	0.14462	0.257	108.60
	KN3	4.841647e+03	5.19e+00	11.864	0.00541	0.258	54.48
Ba	L	0.000000e+00	0.00e+00				
	L3M1*	0.000000e+00	0.00e+00	3.954	0.00707	0.215	84.02
	L2M1*	0.000000e+00	0.00e+00	4.331	0.00273	0.217	15.27
	L3M4*	0.000000e+00	0.00e+00	4.451	0.02360	0.218	3.81
	L3M5*	0.000000e+00	0.00e+00	4.466	0.21590	0.218	3.71
	L2M4*	0.000000e+00	0.00e+00	4.827	0.25873	0.220	7.34
	L1M2*	0.000000e+00	0.00e+00	4.852	0.04847	0.220	6.95
	L1M3*	0.000000e+00	0.00e+00	4.927	0.08442	0.221	6.05
	L3N1*	0.000000e+00	0.00e+00	4.994	0.00528	0.221	5.55
	L3N5*	0.000000e+00	0.00e+00	5.157	0.12205	0.222	4.54
	L1M4*	0.000000e+00	0.00e+00	5.193	0.00129	0.222	4.20
	L1M5*	0.000000e+00	0.00e+00	5.212	0.00325	0.222	4.59
	L3P1*	0.000000e+00	0.00e+00	5.247	0.00013	0.223	5.92
	L2N1*	0.000000e+00	0.00e+00	5.371	0.00357	0.223	9.91
	L2N4*	0.000000e+00	0.00e+00	5.531	0.10994	0.224	25.05
	L2O1*	0.000000e+00	0.00e+00	5.595	0.00081	0.225	25.13
	L1N2*	0.000000e+00	0.00e+00	5.797	0.03645	0.226	28.63
	L1N3*	0.000000e+00	0.00e+00	5.809	0.05890	0.226	27.77
	L1N5*	0.000000e+00	0.00e+00	5.898	0.00095	0.226	43.01

PyMCA : Advanced Fit Results

	L1O3*	0.000000e+00	0.00e+00	5.973	0.01646	0.227	68.08
La	L	8.303147e+03	2.58e+02				
	L3M1*	2.457257e+01	7.64e-01	4.121	0.00296	0.216	44.05
	L2M1*	2.535837e+01	7.88e-01	4.529	0.00305	0.218	4.19
	L3M4*	2.035067e+02	6.33e+00	4.634	0.02451	0.219	5.70
	L3M5*	1.859013e+03	5.78e+01	4.651	0.22389	0.219	5.87
	L2M4*	2.201438e+03	6.84e+01	5.042	0.26513	0.221	5.76
	L1M2*	3.893849e+02	1.21e+01	5.062	0.04690	0.222	5.65
	L1M3*	6.707397e+02	2.08e+01	5.143	0.08078	0.222	4.73
	L3N1*	4.421457e+01	1.37e+00	5.212	0.00533	0.222	4.59
	L3N5*	1.016383e+03	3.16e+01	5.384	0.12241	0.223	10.08
	L1M4*	1.043705e+01	3.24e-01	5.418	0.00126	0.224	12.32
	L1M5*	1.590596e+01	4.94e-01	5.435	0.00192	0.224	14.97
	L3O1*	1.099929e+01	3.42e-01	5.450	0.00132	0.224	16.79
	L3O45*	9.979370e+00	3.10e-01	5.483	0.00120	0.224	22.21
	L2N1*	2.919825e+01	9.08e-01	5.620	0.00352	0.225	25.64
	L2N4*	9.136894e+02	2.84e+01	5.792	0.11004	0.226	28.62
	L2O1*	6.889806e+00	2.14e-01	5.858	0.00083	0.226	30.51
	L2O4*	8.604050e+00	2.67e-01	5.891	0.00104	0.226	38.94
	L1N2*	2.771087e+02	8.61e+00	6.061	0.03337	0.227	68.61
	L1N3*	4.451369e+02	1.38e+01	6.075	0.05361	0.227	67.98
	L1N5*	7.506407e+00	2.33e-01	6.167	0.00090	0.228	71.49
	L1O3*	1.330807e+02	4.14e+00	6.252	0.01603	0.228	76.44
Ce	L	1.965356e+04	2.93e+02				
	L3M1*	6.750372e+01	1.01e+00	4.289	0.00343	0.217	24.24
	L2M1*	6.654074e+01	9.94e-01	4.730	0.00339	0.220	7.07
	L3M4*	5.049403e+02	7.54e+00	4.822	0.02569	0.220	7.34
	L3M5*	4.599658e+03	6.87e+01	4.840	0.23404	0.220	7.02
	L2M4*	5.421230e+03	8.10e+01	5.263	0.27584	0.223	6.58
	L1M2*	9.065647e+02	1.35e+01	5.276	0.04613	0.223	7.58
	L1M3*	1.538437e+03	2.30e+01	5.363	0.07828	0.223	9.75
	L3N1*	1.049372e+02	1.57e+00	5.434	0.00534	0.224	14.97
	L3N5*	2.338065e+03	3.49e+01	5.613	0.11896	0.225	25.23
	L1M4*	2.431280e+01	3.63e-01	5.647	0.00124	0.225	26.73
	L1M5*	3.704547e+01	5.53e-01	5.665	0.00188	0.225	27.68
	L3O1*	2.422164e+01	3.62e-01	5.686	0.00123	0.225	28.70
	L2N1*	6.842211e+01	1.02e+00	5.875	0.00348	0.226	32.46
	L2N4*	2.104062e+03	3.14e+01	6.054	0.10706	0.227	69.33
	L2O1*	1.504390e+01	2.25e-01	6.126	0.00077	0.228	66.29
	L1N2*	5.997824e+02	8.96e+00	6.325	0.03052	0.229	73.78
	L1N3*	9.543153e+02	1.43e+01	6.342	0.04856	0.229	75.28
	L1N5*	1.660771e+01	2.48e-01	6.439	0.00085	0.229	70.87
	L1O3*	2.618664e+02	3.91e+00	6.529	0.01332	0.230	38.60
Nd	L	0.000000e+00	0.00e+00				
	L3M1*	0.000000e+00	0.00e+00	4.633	0.00431	0.219	5.70
	L2M1*	0.000000e+00	0.00e+00	5.146	0.00395	0.222	4.72
	L3M4*	0.000000e+00	0.00e+00	5.208	0.02725	0.222	4.59
	L3M5*	0.000000e+00	0.00e+00	5.230	0.24892	0.222	5.14
	L2M4*	0.000000e+00	0.00e+00	5.722	0.33195	0.225	29.61
	L1M3*	0.000000e+00	0.00e+00	5.829	0.07262	0.226	27.70
	L3N1*	0.000000e+00	0.00e+00	5.893	0.00533	0.226	38.94
	L3N5*	0.000000e+00	0.00e+00	6.090	0.11496	0.227	66.46
	L1M4*	0.000000e+00	0.00e+00	6.126	0.00119	0.228	66.29
	L1M5*	0.000000e+00	0.00e+00	6.148	0.00182	0.228	69.22
	L3O1*	0.000000e+00	0.00e+00	6.170	0.00118	0.228	71.49
	L2N1*	0.000000e+00	0.00e+00	6.406	0.00340	0.229	74.61
	L2N4*	0.000000e+00	0.00e+00	6.604	0.10394	0.230	24.29
	L2O1*	0.000000e+00	0.00e+00	6.684	0.00072	0.231	25.65
	L1N2*	0.000000e+00	0.00e+00	6.883	0.02609	0.232	12.69
	L1N3*	0.000000e+00	0.00e+00	6.901	0.04078	0.232	12.96
	L1N5*	0.000000e+00	0.00e+00	7.009	0.00077	0.232	11.46
	L1O3*	0.000000e+00	0.00e+00	7.105	0.01084	0.233	9.43
Eu	L	5.459378e+03	1.15e+03				

PyMCA : Advanced Fit Results

	L3M1*	3.059120e+01	6.42e+00	5.177	0.00560	0.222	4.23
	L3M4*	1.852914e+02	3.89e+01	5.816	0.03394	0.226	27.76
	L3M5*	1.453289e+03	3.05e+02	5.846	0.26620	0.226	27.62
	L1M2*	2.221741e+02	4.66e+01	6.438	0.04070	0.229	70.87
	L2M4*	1.659827e+03	3.48e+02	6.457	0.30403	0.229	67.27
	L1M3*	3.536593e+02	7.42e+01	6.571	0.06478	0.230	27.51
	L3N1*	2.917295e+01	6.12e+00	6.617	0.00534	0.230	24.17
	L3N5*	5.988210e+02	1.26e+02	6.844	0.10969	0.232	12.38
	L1M4*	6.280125e+00	1.32e+00	6.891	0.00115	0.232	12.96
	L1M5*	9.569690e+00	2.01e+00	6.921	0.00175	0.232	12.61
	L3O1*	6.182355e+00	1.30e+00	6.945	0.00113	0.232	12.16
	L3P1*	9.482964e-01	1.99e-01	6.977	0.00017	0.232	11.49
	L2N1*	1.788885e+01	3.76e+00	7.257	0.00328	0.234	3.63
	L2N4*	5.430315e+02	1.14e+02	7.484	0.09947	0.235	2.71
	L2O1*	3.658052e+00	7.68e-01	7.585	0.00067	0.236	2.30
	L1N2*	1.153473e+02	2.42e+01	7.768	0.02113	0.237	2.59
	L1N3*	1.753036e+02	3.68e+01	7.795	0.03211	0.237	2.70
	L1N5*	3.711487e+00	7.79e-01	7.919	0.00068	0.237	2.44
	L1O3*	4.462966e+01	9.37e+00	8.030	0.00817	0.238	2.25
Gd	L	1.365862e+04	5.06e+02				
	L3M1*	8.196599e+01	3.03e+00	5.362	0.00600	0.223	9.92
	L3M4*	4.046996e+02	1.50e+01	6.026	0.02963	0.227	73.42
	L3M5*	3.751133e+03	1.39e+02	6.057	0.27463	0.227	68.61
	L2M3*	2.107313e+00	7.80e-02	6.386	0.00015	0.229	75.17
	L1M2*	5.397898e+02	2.00e+01	6.687	0.03952	0.231	25.65
	L2M4*	4.198110e+03	1.55e+02	6.713	0.30736	0.231	24.47
	L1M3*	8.482229e+02	3.14e+01	6.832	0.06210	0.232	12.48
	L3N1*	7.313967e+01	2.71e+00	6.867	0.00535	0.232	12.56
	L3N5*	1.483779e+03	5.49e+01	7.102	0.10863	0.233	9.43
	L1M4*	1.548591e+01	5.73e-01	7.158	0.00113	0.233	7.58
	L1M5*	2.360111e+01	8.73e-01	7.190	0.00173	0.233	6.30
	L3O1*	1.565536e+01	5.79e-01	7.207	0.00115	0.234	5.37
	L3O45*	1.195042e+01	4.42e-01	7.243	0.00087	0.234	3.68
	L2N1*	4.355727e+01	1.61e+00	7.554	0.00319	0.235	2.40
	L2N4*	1.347858e+03	4.99e+01	7.790	0.09868	0.237	2.67
	L2O1*	9.105627e+00	3.37e-01	7.894	0.00067	0.237	2.50
	L2O4*	1.039942e+01	3.85e-01	7.930	0.00076	0.238	2.33
	L1N2*	2.720388e+02	1.01e+01	8.087	0.01992	0.238	2.33
	L1N3*	4.074345e+02	1.51e+01	8.105	0.02983	0.238	2.38
	L1N5*	9.039876e+00	3.35e-01	8.235	0.00066	0.239	2.28
	L1O3*	1.095448e+02	4.05e+00	8.355	0.00802	0.240	1.90
Dy	L	1.983017e+03	6.02e+02				
	L3M1*	1.360405e+01	4.13e+00	5.743	0.00686	0.225	29.84
	L3M4*	6.123120e+01	1.86e+01	6.458	0.03088	0.229	67.27
	L3M5*	5.563674e+02	1.69e+02	6.495	0.28057	0.230	52.28
	L2M1*	1.071200e+01	3.25e+00	6.534	0.00540	0.230	38.26
	L2M3*	3.495894e-01	1.06e-01	6.905	0.00018	0.232	12.96
	L1M2*	7.495959e+01	2.27e+01	7.204	0.03780	0.234	5.46
	L2M4*	6.277965e+02	1.91e+02	7.248	0.31659	0.234	3.65
	L1M3*	1.251371e+02	3.80e+01	7.371	0.06310	0.234	3.21
	L3N5*	2.079604e+02	6.31e+01	7.636	0.10487	0.236	2.42
	L1M4*	2.220174e+00	6.74e-01	7.713	0.00112	0.236	2.61
	L3O1*	2.093080e+00	6.35e-01	7.727	0.00106	0.236	2.62
	L1M5*	3.382694e+00	1.03e+00	7.751	0.00171	0.237	2.56
	L3N7*	4.339664e-01	1.32e-01	7.788	0.00022	0.237	2.64
	L2N1*	6.194692e+00	1.88e+00	8.164	0.00312	0.239	2.32
	L2N4*	1.893497e+02	5.75e+01	8.426	0.09549	0.240	1.95
	L2O1*	1.190712e+00	3.61e-01	8.518	0.00060	0.241	2.17
	L1N2*	3.490060e+01	1.06e+01	8.714	0.01760	0.242	2.21
	L1N3*	5.134744e+01	1.56e+01	8.753	0.02589	0.242	2.57
	L1N5*	1.223978e+00	3.71e-01	8.892	0.00062	0.243	2.59
	L1O3*	1.256198e+01	3.81e+00	9.020	0.00633	0.243	2.63
Er	L	1.494687e+03	3.19e+02				

PyMCA : Advanced Fit Results

	L3M1*	1.164044e+01	2.48e+00	6.151	0.00779	0.228	69.22
	L3M4*	4.763458e+01	1.02e+01	6.905	0.03187	0.232	12.96
	L3M5*	4.330328e+02	9.24e+01	6.949	0.28971	0.232	12.00
	L2M1*	8.653160e+00	1.85e+00	7.058	0.00579	0.233	11.31
	L2M3*	2.931589e-01	6.25e-02	7.453	0.00020	0.235	3.05
	L1M2*	5.549488e+01	1.18e+01	7.746	0.03713	0.237	2.60
	L2M4*	4.778710e+02	1.02e+02	7.811	0.31971	0.237	2.67
	L3N1*	8.115021e+00	1.73e+00	7.909	0.00543	0.237	2.43
	L1M3*	8.242127e+01	1.76e+01	7.940	0.05514	0.238	2.27
	L3N5*	1.528776e+02	3.26e+01	8.189	0.10228	0.239	2.41
	L1M4*	3.257595e+00	6.95e-01	8.298	0.00218	0.239	2.01
	L1M5*	2.603468e+00	5.55e-01	8.342	0.00174	0.240	1.91
	L3N7*	3.859492e-01	8.23e-02	8.355	0.00026	0.240	1.90
	L2N1*	4.592511e+00	9.80e-01	8.815	0.00307	0.242	2.51
	L2N4*	1.368133e+02	2.92e+01	9.088	0.09153	0.244	2.39
	L2O1*	8.445182e-01	1.80e-01	9.205	0.00057	0.244	2.29
	L2N6*	2.708003e-01	5.78e-02	9.261	0.00018	0.245	2.45
	L1N2*	2.405910e+01	5.13e+00	9.385	0.01610	0.245	2.24
	L1N3*	3.469092e+01	7.40e+00	9.431	0.02321	0.245	2.24
	L1N5*	8.908160e-01	1.90e-01	9.580	0.00060	0.246	2.78
	L1O3*	8.243717e+00	1.76e+00	9.722	0.00552	0.247	6.70
Tm	L	5.971506e+02	4.83e+02				
	L3M1*	4.874783e+00	3.94e+00	6.341	0.00816	0.229	75.28
	L3M4*	1.940946e+01	1.57e+01	7.133	0.03250	0.233	8.38
	L3M5*	1.760139e+02	1.42e+02	7.180	0.29476	0.233	6.63
	L2M1*	3.511411e+00	2.84e+00	7.310	0.00588	0.234	3.12
	L2M3*	1.223509e-01	9.89e-02	7.732	0.00020	0.236	2.68
	L1M2*	2.214587e+01	1.79e+01	8.026	0.03709	0.238	2.23
	L2M4*	1.908950e+02	1.54e+02	8.102	0.31968	0.238	2.34
	L3N1*	3.268976e+00	2.64e+00	8.176	0.00547	0.239	2.32
	L1M3*	3.242266e+01	2.62e+01	8.231	0.05430	0.239	2.32
	L3N5*	6.055784e+01	4.90e+01	8.468	0.10141	0.240	2.15
	L1M4*	1.313985e+00	1.06e+00	8.598	0.00220	0.241	1.82
	L1M5*	1.226977e+00	9.92e-01	8.647	0.00205	0.241	2.05
	L2N1*	1.795002e+00	1.45e+00	9.145	0.00301	0.244	2.22
	L2N4*	5.326280e+01	4.31e+01	9.437	0.08919	0.246	2.23
	L2O1*	3.252289e-01	2.63e-01	9.564	0.00054	0.246	2.59
	L2N6*	1.160729e-01	9.38e-02	9.613	0.00019	0.246	3.32
	L1N2*	9.269271e+00	7.49e+00	9.730	0.01552	0.247	7.06
	L1N3*	1.317322e+01	1.07e+01	9.779	0.02206	0.247	9.92
	L1N5*	3.518796e-01	2.85e-01	9.936	0.00059	0.248	63.34
	L1O3*	3.093921e+00	2.50e+00	10.083	0.00518	0.249	283.58
Yb	L	7.710416e+03	3.31e+02				
	L3M1*	6.667442e+01	2.86e+00	6.546	0.00865	0.230	35.52
	L3M4*	2.551627e+02	1.09e+01	7.367	0.03309	0.234	3.21
	L3M5*	2.314165e+03	9.92e+01	7.416	0.30013	0.235	3.49
	L2M1*	4.614356e+01	1.98e+00	7.580	0.00598	0.236	2.31
	L2M3*	1.649143e+00	7.07e-02	8.028	0.00021	0.238	2.25
	L1M2*	2.868914e+02	1.23e+01	8.313	0.03721	0.240	2.01
	L2M4*	2.461060e+03	1.06e+02	8.402	0.31919	0.240	1.93
	L3N1*	4.280928e+01	1.84e+00	8.456	0.00555	0.240	1.96
	L1M3*	4.138768e+02	1.77e+01	8.537	0.05368	0.241	2.30
	L3N4*	7.775546e+01	3.33e+00	8.745	0.01008	0.242	2.56
	L3N5*	6.988529e+02	3.00e+01	8.759	0.09064	0.242	2.61
	L3O1*	7.950986e+00	3.41e-01	8.889	0.00103	0.243	2.59
	L1M4*	9.037392e+00	3.87e-01	8.910	0.00117	0.243	2.59
	L3N7*	2.360418e+00	1.01e-01	8.939	0.00031	0.243	2.57
	L1M5*	1.390339e+01	5.96e-01	8.959	0.00180	0.243	2.63
	L2N1*	2.259315e+01	9.69e-01	9.491	0.00293	0.246	2.17
	L2N4*	6.642073e+02	2.85e+01	9.780	0.08614	0.247	9.92
	L2O1*	4.018121e+00	1.72e-01	9.924	0.00052	0.248	52.95
	L2N6*	1.594964e+00	6.84e-02	9.973	0.00021	0.248	115.67
	L1N2*	1.154128e+02	4.95e+00	10.090	0.01497	0.249	284.81

PyMCA : Advanced Fit Results

	L1N3*	1.621568e+02	6.95e+00	10.143	0.02103	0.249	295.54
	L1N4*	1.759782e+00	7.54e-02	10.288	0.00023	0.250	376.56
	L1N5*	2.735483e+00	1.17e-01	10.301	0.00035	0.250	377.53
	L1O3*	3.764502e+01	1.61e+00	10.463	0.00488	0.251	411.87
Lu	L	3.434955e+03	3.23e+02				
	L3M1*	3.098783e+01	2.91e+00	6.753	0.00902	0.231	20.57
	L3M4*	1.146353e+02	1.08e+01	7.605	0.03337	0.236	2.30
	L3M5*	1.037879e+03	9.75e+01	7.656	0.30215	0.236	2.41
	L2M1*	2.122180e+01	1.99e+00	7.857	0.00618	0.237	2.62
	L2M3*	7.772000e-01	7.30e-02	8.325	0.00023	0.240	2.00
	L1M2*	1.246040e+02	1.17e+01	8.607	0.03628	0.241	1.84
	L2M4*	1.110326e+03	1.04e+02	8.709	0.32324	0.242	2.25
	L3N1*	1.909411e+01	1.79e+00	8.738	0.00556	0.242	2.60
	L1M3*	1.768574e+02	1.66e+01	8.847	0.05149	0.242	2.46
	L3N5*	3.417503e+02	3.21e+01	9.048	0.09949	0.243	2.60
	L3O1*	3.628195e+00	3.41e-01	9.187	0.00106	0.244	2.34
	L1M4*	6.688483e+00	6.28e-01	9.234	0.00195	0.244	2.56
	L1M5*	6.136687e+00	5.76e-01	9.282	0.00179	0.245	2.57
	L2N1*	9.952802e+00	9.35e-01	9.842	0.00290	0.248	15.84
	L2N4*	2.925775e+02	2.75e+01	10.144	0.08518	0.249	295.54
	L2O1*	1.811190e+00	1.70e-01	10.292	0.00053	0.250	376.56
	L2O4*	2.115405e+00	1.99e-01	10.344	0.00062	0.250	377.16
	L1N2*	4.842127e+01	4.55e+00	10.460	0.01410	0.251	414.47
Hf	L1N3*	6.720113e+01	6.31e+00	10.511	0.01956	0.251	417.38
	L1N5*	1.941336e+00	1.82e-01	10.672	0.00057	0.252	226.67
	L1O3*	1.634741e+01	1.54e+00	10.842	0.00476	0.253	130.61
	L	0.000000e+00	0.00e+00				
	L3M1*	0.000000e+00	0.00e+00	6.960	0.00942	0.232	11.77
	L3M4*	0.000000e+00	0.00e+00	7.844	0.03365	0.237	2.75
	L3M5*	0.000000e+00	0.00e+00	7.899	0.30447	0.237	2.49
	L2M1*	0.000000e+00	0.00e+00	8.139	0.00623	0.239	2.26
	L2M3*	0.000000e+00	0.00e+00	8.632	0.00024	0.241	2.01
	L1M2*	0.000000e+00	0.00e+00	8.905	0.03534	0.243	2.60
	L2M4*	0.000000e+00	0.00e+00	9.023	0.33205	0.243	2.63
	L1M3*	0.000000e+00	0.00e+00	9.163	0.04930	0.244	2.25
	L3N4*	0.000000e+00	0.00e+00	9.337	0.00987	0.245	2.58
	L3N5*	0.000000e+00	0.00e+00	9.347	0.08863	0.245	2.35
	L3O1*	0.000000e+00	0.00e+00	9.496	0.00108	0.246	2.14
	L3N7*	0.000000e+00	0.00e+00	9.544	0.00027	0.246	2.41
	L1M4*	0.000000e+00	0.00e+00	9.554	0.00231	0.246	2.45
	L1M5*	0.000000e+00	0.00e+00	9.609	0.00177	0.246	3.19
	L2N1*	0.000000e+00	0.00e+00	10.201	0.00287	0.249	313.69
	L2N4*	0.000000e+00	0.00e+00	10.516	0.08419	0.251	415.09
	L2O1*	0.000000e+00	0.00e+00	10.675	0.00053	0.252	214.32
	L2N6*	0.000000e+00	0.00e+00	10.722	0.00020	0.252	165.10
Scatter	L2O4*	0.000000e+00	0.00e+00	10.733	0.00098	0.252	159.53
	L1N2*	0.000000e+00	0.00e+00	10.834	0.01327	0.253	137.65
	L1N3*	0.000000e+00	0.00e+00	10.890	0.01817	0.253	85.61
	L1N4*	0.000000e+00	0.00e+00	11.047	0.00021	0.254	48.47
	L1N5*	0.000000e+00	0.00e+00	11.057	0.00033	0.254	44.89
	L1O3*	0.000000e+00	0.00e+00	11.237	0.00462	0.255	76.17
	Peak000	0.000000e+00	0.00e+00				
Scatter	Scatter 000	0.000000e+00	0.00e+00	13.500	1.00000	0.266	9.10
	Compton000	1.021370e+04	4.76e+02				
	Scatter 000	1.021370e+04	4.76e+02	13.153	1.00000	0.264	11.87

created: Mon Mar 03 14:50:53 2014

last modified: Mon Mar 03 14:50:53 2014 by mbexjja4

PyMCA : Advanced Fit Results

| [PyMCA home](#) | [ESRF home](#) | [BLISS home](#) | [Concentrations](#) | [Fit Peak Results](#)

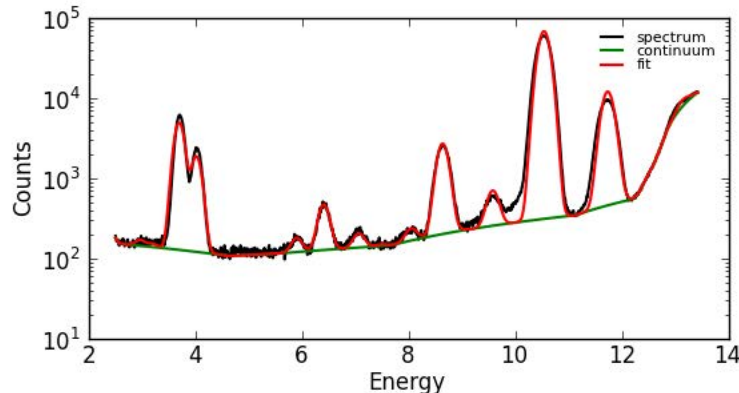
Computed File : C:/Users/mbexjja4/Documents/PhDResearch/Manuscripts/Interface/Revision1/M13_DINOBIRD_BIRDGL

Source : [C:/Users/mbexjja4/Documents/PhDResearch/SSRL_Mar2013/Mar 2013 Final Package/M13_Spectra/M13_DINOBIRD_BIRDGL_PATH2_HZ.mca]

Selection : M13_DINOBIRD_BIRDGL_PATH2_HZ.mca 2.1.1.1

Parameters : [M13_DINOBIRD_BIRDGL_PATH2_HZ.mca_2.1.1.1.txt](#)

Spectrum, Continuum and Fitted values :



Fit Parameters :

FIT parameters	
Region of Fit	250 - 1345
Number of iterations	1
Chi square	99.7477
Last Chi square difference	10842579.3793 %
Calibration parameters	
Zero	4.30438E-03 +/- 4.30438E-03
Gain	9.97000E-03 +/- 9.97000E-03
Noise	1.90000E-01 +/- 1.90000E-01
Fano	1.20000E-01 +/- 1.20000E-01
Sum	0.00000E+00 +/- 0.00000E+00
Continuum parameters	
Type	Strip Background
Strip Constant	1.00000
Strip Iterations	20000
Strip Width	4
Smoothing Filter Width	10

Concentrations:

Element	Group	Fit Area	Sigma Area	M	a s s f r a c t i o n	Layer0
P	K	0.000000e+00	0.00e+00	0	0	
Ar	K	8.994814e+02	9.01e+01	0.1584	0.1584	
Ca	K	1.508179e+05	4.02e+02	0.2816	0.2816	
Mn	K	1.783545e+03	9.24e+01	4.935e-05	4.935e-05	
Fe	K	9.978076e+03	1.36e+02	0.0001447	0.0001447	
Ni	K	2.563857e+02	8.62e+01	1.312e-06	1.312e-06	
Cu	K	2.119079e+03	1.04e+02	7.462e-06	7.462e-06	
Zn	K	7.690776e+04	3.07e+02	0.0001856	0.0001856	
As	K	2.173880e+06	1.49e+03	0.002332	0.002332	

Fit Peak Results:

Element	Group	Fit Area	Sigma	Energy	Ratio	FWHM	Chi square
P	K	0.000000e+00	0.00e+00				
	KL3	0.000000e+00	0.00e+00	2.010	0.42423	0.203	0.00

	KM3	0.000000e+00	0.00e+00	2.136	0.57577	0.204	0.00
Ar	K	8.994814e+02	9.01e+01				0.84
	KL3	5.911520e+02	5.92e+01	2.957	0.65721	0.209	
	KM3	3.083294e+02	3.09e+01	3.190	0.34279	0.210	3.59
Ca	K	1.508179e+05	4.02e+02				
	KL3	1.102725e+05	2.94e+02	3.691	0.73116	0.213	159.70
	KM3	4.054537e+04	1.08e+02	4.013	0.26884	0.215	52.88
Mn	K	1.783545e+03	9.24e+01				
	KL2	4.896251e+02	2.54e+01	5.888	0.27452	0.226	1.16
	KL3	9.707326e+02	5.03e+01	5.899	0.54427	0.226	1.12
	KM3	3.231873e+02	1.67e+01	6.490	0.18121	0.230	1.24
Fe	K	9.978076e+03	1.36e+02				
	KL2	2.768737e+03	3.78e+01	6.391	0.27748	0.229	1.42
	KL3	5.476909e+03	7.48e+01	6.404	0.54889	0.229	1.40
	KM3	1.732430e+03	2.37e+01	7.058	0.17362	0.233	1.45
Ni	K	2.563857e+02	8.62e+01				
	KL2	7.225057e+01	2.43e+01	7.461	0.28180	0.235	0.90
	KL3	1.424187e+02	4.79e+01	7.478	0.55549	0.235	0.93
	KM3	4.171644e+01	1.40e+01	8.265	0.16271	0.239	3.12
Cu	K	2.119079e+03	1.04e+02				
	KL2	6.030474e+02	2.97e+01	8.028	0.28458	0.238	1.48
	KL3	1.185185e+03	5.83e+01	8.048	0.55929	0.238	1.58
	KM3	3.308470e+02	1.63e+01	8.905	0.15613	0.243	8.06
Zn	K	7.690776e+04	3.07e+02				
	KL2	2.197816e+04	8.78e+01	8.616	0.28577	0.241	8.69
	KL3	4.312200e+04	1.72e+02	8.639	0.56070	0.241	8.86
	KM3	1.180760e+04	4.72e+01	9.572	0.15353	0.246	12.66
As	K	2.173880e+06	1.49e+03				
	KL2	6.258824e+05	4.29e+02	10.508	0.28791	0.251	1069.52
	KL3	1.221855e+06	8.37e+02	10.544	0.56206	0.251	1024.24
	KM3	3.143757e+05	2.15e+02	11.724	0.14462	0.257	279.85
	KN3	1.176782e+04	8.06e+00	11.864	0.00541	0.258	171.38
Scatter	Peak000	0.000000e+00	0.00e+00				
	Scatter 000	0.000000e+00	0.00e+00	13.500	1.00000	0.266	15.37
Scatter	Compton000	4.434014e+04	6.09e+02				
	Scatter 000	4.434014e+04	6.09e+02	13.153	1.00000	0.264	31.84

created: Fri Mar 07 17:00:31 2014

last modified: Fri Mar 07 17:00:31 2014 by mbexjja4

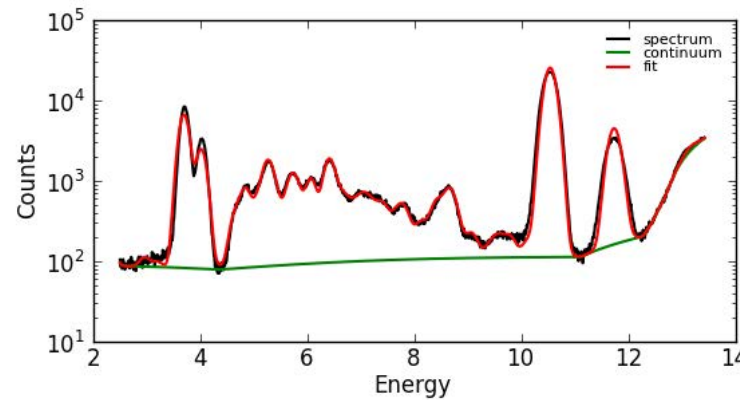
PyMCA : Advanced Fit Results

| [PyMCA home](#) | [ESRF home](#) | [BLISS home](#) | [Concentrations](#) | [Fit Peak Results](#)

Computed File : C:/Users/mbexjja4/Documents/PhDResearch/Manuscripts/Interface/Revision1/durango11_HZ.mca

Source : [C:/Users/mbexjja4/Documents/PhDResearch/SSRL_Mar2013/Mar 2013 Final Package/M13_Spectra/durango11_HZ.mca]
 Selection : durango11_HZ.mca 2.1.1.1
 Parameters : [durango11_HZ.mca_2.1.1.1.txt](#)

Spectrum, Continuum and Fitted values :



Fit Parameters :

FIT parameters	
Region of Fit	250 - 1345
Number of iterations	2
Chi square	49.2499
Last Chi square difference	5309133.8822 %
Calibration parameters	
Zero	4.30438E-03 +/- 4.30438E-03
Gain	9.97000E-03 +/- 9.97000E-03
Noise	1.90000E-01 +/- 1.90000E-01
Fano	1.20000E-01 +/- 1.20000E-01
Sum	0.00000E+00 +/- 0.00000E+00
Continuum parameters	
Type	Strip Background
Strip Constant	1.00000
Strip Iterations	20000
Strip Width	4
Smoothing Filter Width	10

Concentrations:

Element	Group	Fit Area	Sigma Area	M	a s s f r a c t i o n	Layer0
P	K	0.000000e+00	0.00e+00	0	0	
Ar	K	9.080615e+02	7.20e+01	0.16	0.16	
Ca	K	2.045934e+05	4.61e+02	0.382	0.382	
Cr	K	6.074011e+03	2.61e+02	0.0003404	0.0003404	
Fe	K	4.021491e+04	3.87e+02	0.0005834	0.0005834	
Co	K	0.000000e+00	0.00e+00	0	0	
Zn	K	1.336714e+04	2.40e+02	3.226e-05	3.226e-05	
As	K	8.109976e+05	9.10e+02	0.00087	0.00087	
Ba	L	0.000000e+00	0.00e+00	0	0	
La	L	2.626315e+04	3.66e+02	0.005094	0.005094	
Ce	L	6.091691e+04	5.91e+02	0.007852	0.007852	

Nd	L	5.534620e+04	6.07e+02	0.003437	0.003437
Eu	L	6.750183e+03	6.69e+02	0.0001656	0.0001656
Gd	L	2.445765e+04	3.87e+02	0.0004624	0.0004624
Dy	L	1.537014e+04	4.60e+02	0.0001758	0.0001758
Er	L	1.358579e+04	3.73e+02	9.929e-05	9.929e-05
Tm	L	6.668889e+03	2.88e+02	3.964e-05	3.964e-05
Yb	L	2.352992e+04	3.31e+02	0.0001165	0.0001165
Lu	L	1.290919e+04	3.60e+02	5.241e-05	5.241e-05
Hf	L	8.545040e+02	2.41e+02	2.904e-06	2.904e-06

Fit Peak Results:

Element	Group	Fit Area	Sigma	Energy	Ratio	FWHM	Chi square
P	K	0.000000e+00	0.00e+00				
	KL3	0.000000e+00	0.00e+00	2.010	0.42423	0.203	0.00
	KM3	0.000000e+00	0.00e+00	2.136	0.57577	0.204	0.00
Ar	K	9.080615e+02	7.20e+01				
	KL3	5.967910e+02	4.73e+01	2.957	0.65721	0.209	1.38
	KM3	3.112705e+02	2.47e+01	3.190	0.34279	0.210	5.65
Ca	K	2.045934e+05	4.61e+02				
	KL3	1.495912e+05	3.37e+02	3.691	0.73116	0.213	259.56
	KM3	5.500222e+04	1.24e+02	4.013	0.26884	0.215	96.28
Cr	K	6.074011e+03	2.61e+02				
	KL3	4.952902e+03	2.13e+02	5.412	0.81543	0.224	6.16
	KM3	1.121109e+03	4.81e+01	5.947	0.18457	0.227	5.41
Fe	K	4.021491e+04	3.87e+02				
	KL2	1.115891e+04	1.07e+02	6.391	0.27748	0.229	7.37
	KL3	2.207373e+04	2.12e+02	6.404	0.54889	0.229	7.34
	KM3	6.982260e+03	6.72e+01	7.058	0.17362	0.233	3.21
Co	K	0.000000e+00	0.00e+00				
	KL2	0.000000e+00	0.00e+00	6.915	0.27986	0.232	2.37
	KL3	0.000000e+00	0.00e+00	6.930	0.55248	0.232	2.42
	KM3	0.000000e+00	0.00e+00	7.649	0.16766	0.236	2.88
Zn	K	1.336714e+04	2.40e+02				
	KL2	3.819967e+03	6.87e+01	8.616	0.28577	0.241	3.32
	KL3	7.494922e+03	1.35e+02	8.639	0.56070	0.241	3.14
	KM3	2.052248e+03	3.69e+01	9.572	0.15353	0.246	1.08
As	K	8.109976e+05	9.10e+02				
	KL2	2.334945e+05	2.62e+02	10.508	0.28791	0.251	377.77
	KL3	4.558306e+05	5.11e+02	10.544	0.56206	0.251	366.22
	KM3	1.172824e+05	1.32e+02	11.724	0.14462	0.257	120.80
	KN3	4.390157e+03	4.92e+00	11.864	0.00541	0.258	92.21
Ba	L	0.000000e+00	0.00e+00				
	L3M1*	0.000000e+00	0.00e+00	3.954	0.00707	0.215	133.22
	L2M1*	0.000000e+00	0.00e+00	4.331	0.00273	0.217	25.57
	L3M4*	0.000000e+00	0.00e+00	4.451	0.02360	0.218	7.40
	L3M5*	0.000000e+00	0.00e+00	4.466	0.21590	0.218	7.67
	L2M4*	0.000000e+00	0.00e+00	4.827	0.25873	0.220	6.15
	L1M2*	0.000000e+00	0.00e+00	4.852	0.04847	0.220	5.98
	L1M3*	0.000000e+00	0.00e+00	4.927	0.08442	0.221	7.56
	L3N1*	0.000000e+00	0.00e+00	4.994	0.00528	0.221	8.32
	L3N5*	0.000000e+00	0.00e+00	5.157	0.12205	0.222	7.58
	L1M4*	0.000000e+00	0.00e+00	5.193	0.00129	0.222	7.27
	L1M5*	0.000000e+00	0.00e+00	5.212	0.00325	0.222	7.35
	L3P1*	0.000000e+00	0.00e+00	5.247	0.00013	0.223	7.26
	L2N1*	0.000000e+00	0.00e+00	5.371	0.00357	0.223	6.11
	L2N4*	0.000000e+00	0.00e+00	5.531	0.10994	0.224	3.69
	L2O1*	0.000000e+00	0.00e+00	5.595	0.00081	0.225	3.48
	L1N2*	0.000000e+00	0.00e+00	5.797	0.03645	0.226	3.67
	L1N3*	0.000000e+00	0.00e+00	5.809	0.05890	0.226	3.63
	L1N5*	0.000000e+00	0.00e+00	5.898	0.00095	0.226	3.96
	L1O3*	0.000000e+00	0.00e+00	5.973	0.01646	0.227	6.23

PyMCA : Advanced Fit Results

La	L	2.626315e+04	3.66e+02				
	L3M1*	7.772390e+01	1.08e+00	4.121	0.00296	0.216	72.94
	L2M1*	8.020942e+01	1.12e+00	4.529	0.00305	0.218	6.28
	L3M4*	6.436990e+02	8.96e+00	4.634	0.02451	0.219	5.16
	L3M5*	5.880124e+03	8.19e+01	4.651	0.22389	0.219	5.16
	L2M4*	6.963226e+03	9.70e+01	5.042	0.26513	0.221	7.80
	L1M2*	1.231638e+03	1.71e+01	5.062	0.04690	0.222	7.45
	L1M3*	2.121573e+03	2.95e+01	5.143	0.08078	0.222	7.78
	L3N1*	1.398522e+02	1.95e+00	5.212	0.00533	0.222	7.35
	L3N5*	3.214855e+03	4.48e+01	5.384	0.12241	0.223	6.19
	L1M4*	3.301277e+01	4.60e-01	5.418	0.00126	0.224	6.07
	L1M5*	5.031111e+01	7.01e-01	5.435	0.00192	0.224	5.84
	L3O1*	3.479114e+01	4.84e-01	5.450	0.00132	0.224	5.77
	L3O45*	3.156510e+01	4.40e-01	5.483	0.00120	0.224	4.68
	L2N1*	9.235510e+01	1.29e+00	5.620	0.00352	0.225	3.58
	L2N4*	2.890032e+03	4.02e+01	5.792	0.11004	0.226	3.62
	L2O1*	2.179270e+01	3.03e-01	5.858	0.00083	0.226	3.37
	L2O4*	2.721491e+01	3.79e-01	5.891	0.00104	0.226	3.73
	L1N2*	8.765047e+02	1.22e+01	6.061	0.03337	0.227	7.06
	L1N3*	1.407984e+03	1.96e+01	6.075	0.05361	0.227	7.10
	L1N5*	2.374303e+01	3.31e-01	6.167	0.00090	0.228	7.56
	L1O3*	4.209389e+02	5.86e+00	6.252	0.01603	0.228	7.29
Ce	L	6.091691e+04	5.91e+02				
	L3M1*	2.092302e+02	2.03e+00	4.289	0.00343	0.217	43.14
	L2M1*	2.062454e+02	2.00e+00	4.730	0.00339	0.220	6.12
	L3M4*	1.565081e+03	1.52e+01	4.822	0.02569	0.220	6.15
	L3M5*	1.425681e+04	1.38e+02	4.840	0.23404	0.220	5.94
	L2M4*	1.680330e+04	1.63e+02	5.263	0.27584	0.223	7.24
	L1M2*	2.809930e+03	2.73e+01	5.276	0.04613	0.223	7.12
	L1M3*	4.768440e+03	4.63e+01	5.363	0.07828	0.223	6.17
	L3N1*	3.252565e+02	3.16e+00	5.434	0.00534	0.224	5.84
	L3N5*	7.246917e+03	7.03e+01	5.613	0.11896	0.225	3.57
	L1M4*	7.535841e+01	7.31e-01	5.647	0.00124	0.225	3.65
	L1M5*	1.148238e+02	1.11e+00	5.665	0.00188	0.225	3.77
	L3O1*	7.507586e+01	7.28e-01	5.686	0.00123	0.225	3.75
	L2N1*	2.120768e+02	2.06e+00	5.875	0.00348	0.226	3.30
	L2N4*	6.521616e+03	6.33e+01	6.054	0.10706	0.227	7.06
	L2O1*	4.662912e+01	4.52e-01	6.126	0.00077	0.228	7.31
	L1N2*	1.859047e+03	1.80e+01	6.325	0.03052	0.229	7.16
	L1N3*	2.957935e+03	2.87e+01	6.342	0.04856	0.229	7.30
	L1N5*	5.147619e+01	4.99e-01	6.439	0.00085	0.229	6.93
	L1O3*	8.116643e+02	7.88e+00	6.529	0.01332	0.230	4.04
Nd	L	5.534620e+04	6.07e+02				
	L3M1*	2.384463e+02	2.62e+00	4.633	0.00431	0.219	5.16
	L2M1*	2.187144e+02	2.40e+00	5.146	0.00395	0.222	7.65
	L3M4*	1.508016e+03	1.65e+01	5.208	0.02725	0.222	7.35
	L3M5*	1.377660e+04	1.51e+02	5.230	0.24892	0.222	7.33
	L2M4*	1.837220e+04	2.02e+02	5.722	0.33195	0.225	3.85
	L1M3*	4.019397e+03	4.41e+01	5.829	0.07262	0.226	3.51
	L3N1*	2.952312e+02	3.24e+00	5.893	0.00533	0.226	3.73
	L3N5*	6.362440e+03	6.98e+01	6.090	0.11496	0.227	7.27
	L1M4*	6.603596e+01	7.25e-01	6.126	0.00119	0.228	7.31
	L1M5*	1.006402e+02	1.10e+00	6.148	0.00182	0.228	7.47
	L3O1*	6.518436e+01	7.15e-01	6.170	0.00118	0.228	7.56
	L2N1*	1.880381e+02	2.06e+00	6.406	0.00340	0.229	7.34
	L2N4*	5.752552e+03	6.31e+01	6.604	0.10394	0.230	2.85
	L2O1*	3.971355e+01	4.36e-01	6.684	0.00072	0.231	2.54
	L1N2*	1.443820e+03	1.58e+01	6.883	0.02609	0.232	2.39
	L1N3*	2.256785e+03	2.48e+01	6.901	0.04078	0.232	2.42
	L1N5*	4.250682e+01	4.66e-01	7.009	0.00077	0.232	3.01
	L1O3*	5.998818e+02	6.58e+00	7.105	0.01084	0.233	2.98
Eu	L	6.750183e+03	6.69e+02				
	L3M1*	3.782413e+01	3.75e+00	5.177	0.00560	0.222	7.26

PyMCA : Advanced Fit Results

	L3M4*	2.291013e+02	2.27e+01	5.816	0.03394	0.226	3.60
	L3M5*	1.796902e+03	1.78e+02	5.846	0.26620	0.226	3.32
	L1M2*	2.747045e+02	2.72e+01	6.438	0.04070	0.229	6.93
	L2M4*	2.052274e+03	2.03e+02	6.457	0.30403	0.229	6.81
	L1M3*	4.372778e+02	4.34e+01	6.571	0.06478	0.230	3.09
	L3N1*	3.607055e+01	3.58e+00	6.617	0.00534	0.230	2.61
	L3N5*	7.404051e+02	7.34e+01	6.844	0.10969	0.232	2.48
	L1M4*	7.764986e+00	7.70e-01	6.891	0.00115	0.232	2.40
	L1M5*	1.183233e+01	1.17e+00	6.921	0.00175	0.232	2.43
	L3O1*	7.644100e+00	7.58e-01	6.945	0.00113	0.232	2.44
	L3P1*	1.172510e+00	1.16e-01	6.977	0.00017	0.232	2.63
	L2N1*	2.211846e+01	2.19e+00	7.257	0.00328	0.234	2.97
	L2N4*	6.714248e+02	6.66e+01	7.484	0.09947	0.235	3.43
	L2O1*	4.522955e+00	4.48e-01	7.585	0.00067	0.236	3.12
	L1N2*	1.426199e+02	1.41e+01	7.768	0.02113	0.237	3.34
	L1N3*	2.167521e+02	2.15e+01	7.795	0.03211	0.237	3.38
	L1N5*	4.589024e+00	4.55e-01	7.919	0.00068	0.237	3.16
	L1O3*	5.518182e+01	5.47e+00	8.030	0.00817	0.238	3.12
Gd	L	2.445765e+04	3.87e+02				
	L3M1*	1.467715e+02	2.32e+00	5.362	0.00600	0.223	6.15
	L3M4*	7.246708e+02	1.15e+01	6.026	0.02963	0.227	6.80
	L3M5*	6.716925e+03	1.06e+02	6.057	0.27463	0.227	7.06
	L2M3*	3.773437e+00	5.96e-02	6.386	0.00015	0.229	7.28
	L1M2*	9.665687e+02	1.53e+01	6.687	0.03952	0.231	2.54
	L2M4*	7.517299e+03	1.19e+02	6.713	0.30736	0.231	2.47
	L1M3*	1.518861e+03	2.40e+01	6.832	0.06210	0.232	2.35
	L3N1*	1.309667e+02	2.07e+00	6.867	0.00535	0.232	2.42
	L3N5*	2.656912e+03	4.20e+01	7.102	0.10863	0.233	2.98
	L1M4*	2.772968e+01	4.38e-01	7.158	0.00113	0.233	2.91
	L1M5*	4.226107e+01	6.68e-01	7.190	0.00173	0.233	3.09
	L3O1*	2.803310e+01	4.43e-01	7.207	0.00115	0.234	3.07
	L3O45*	2.139888e+01	3.38e-01	7.243	0.00087	0.234	3.14
	L2N1*	7.799535e+01	1.23e+00	7.554	0.00319	0.235	3.39
	L2N4*	2.413527e+03	3.81e+01	7.790	0.09868	0.237	3.32
	L2O1*	1.630489e+01	2.58e-01	7.894	0.00067	0.237	3.40
	L2O4*	1.862161e+01	2.94e-01	7.930	0.00076	0.238	3.08
	L1N2*	4.871233e+02	7.70e+00	8.087	0.01992	0.238	3.62
	L1N3*	7.295680e+02	1.15e+01	8.105	0.02983	0.238	3.81
	L1N5*	1.618715e+01	2.56e-01	8.235	0.00066	0.239	3.66
	L1O3*	1.961552e+02	3.10e+00	8.355	0.00802	0.240	2.97
Dy	L	1.537014e+04	4.60e+02				
	L3M1*	1.054434e+02	3.15e+00	5.743	0.00686	0.225	3.76
	L3M4*	4.745960e+02	1.42e+01	6.458	0.03088	0.229	6.81
	L3M5*	4.312340e+03	1.29e+02	6.495	0.28057	0.230	5.64
	L2M1*	8.302747e+01	2.48e+00	6.534	0.00540	0.230	3.97
	L2M3*	2.709627e+00	8.10e-02	6.905	0.00018	0.232	2.42
	L1M2*	5.810032e+02	1.74e+01	7.204	0.03780	0.234	3.06
	L2M4*	4.865978e+03	1.46e+02	7.248	0.31659	0.234	3.09
	L1M3*	9.699234e+02	2.90e+01	7.371	0.06310	0.234	3.16
	L3N5*	1.611877e+03	4.82e+01	7.636	0.10487	0.236	2.83
	L1M4*	1.720832e+01	5.15e-01	7.713	0.00112	0.236	3.49
	L3O1*	1.622322e+01	4.85e-01	7.727	0.00106	0.236	3.50
	L1M5*	2.621887e+01	7.84e-01	7.751	0.00171	0.237	3.49
	L3N7*	3.363624e+00	1.01e-01	7.788	0.00022	0.237	3.33
	L2N1*	4.801435e+01	1.44e+00	8.164	0.00312	0.239	3.79
	L2N4*	1.467628e+03	4.39e+01	8.426	0.09549	0.240	2.99
	L2O1*	9.229075e+00	2.76e-01	8.518	0.00060	0.241	3.21
	L1N2*	2.705106e+02	8.09e+00	8.714	0.01760	0.242	2.70
	L1N3*	3.979881e+02	1.19e+01	8.753	0.02589	0.242	2.58
	L1N5*	9.486914e+00	2.84e-01	8.892	0.00062	0.243	2.58
	L1O3*	9.736644e+01	2.91e+00	9.020	0.00633	0.243	2.78
Er	L	1.358579e+04	3.73e+02				
	L3M1*	1.058045e+02	2.90e+00	6.151	0.00779	0.228	7.47

PyMCA : Advanced Fit Results

	L3M4*	4.329694e+02	1.19e+01	6.905	0.03187	0.232	2.42
	L3M5*	3.936004e+03	1.08e+02	6.949	0.28971	0.232	2.48
	L2M1*	7.865196e+01	2.16e+00	7.058	0.00579	0.233	3.21
	L2M3*	2.664636e+00	7.31e-02	7.453	0.00020	0.235	3.45
	L1M2*	5.044148e+02	1.38e+01	7.746	0.03713	0.237	3.54
	L2M4*	4.343557e+03	1.19e+02	7.811	0.31971	0.237	3.27
	L3N1*	7.376060e+01	2.02e+00	7.909	0.00543	0.237	3.31
	L1M3*	7.491592e+02	2.06e+01	7.940	0.05514	0.238	2.99
	L3N5*	1.389565e+03	3.81e+01	8.189	0.10228	0.239	3.81
	L1M4*	2.960956e+01	8.12e-01	8.298	0.00218	0.239	3.15
	L1M5*	2.366394e+01	6.49e-01	8.342	0.00174	0.240	3.03
	L3N7*	3.508044e+00	9.63e-02	8.355	0.00026	0.240	2.97
	L2N1*	4.174314e+01	1.15e+00	8.815	0.00307	0.242	2.78
	L2N4*	1.243550e+03	3.41e+01	9.088	0.09153	0.244	2.56
	L2O1*	7.676156e+00	2.11e-01	9.205	0.00057	0.244	1.85
	L2N6*	2.461410e+00	6.75e-02	9.261	0.00018	0.245	1.60
	L1N2*	2.186826e+02	6.00e+00	9.385	0.01610	0.245	1.25
	L1N3*	3.153194e+02	8.65e+00	9.431	0.02321	0.245	1.13
	L1N5*	8.096976e+00	2.22e-01	9.580	0.00060	0.246	1.08
	L1O3*	7.493037e+01	2.06e+00	9.722	0.00552	0.247	3.15
Tm	L	6.668889e+03	2.88e+02				
	L3M1*	5.444084e+01	2.35e+00	6.341	0.00816	0.229	7.30
	L3M4*	2.167619e+02	9.37e+00	7.133	0.03250	0.233	2.93
	L3M5*	1.965697e+03	8.50e+01	7.180	0.29476	0.233	3.08
	L2M1*	3.921491e+01	1.70e+00	7.310	0.00588	0.234	3.00
	L2M3*	1.366397e+00	5.91e-02	7.732	0.00020	0.236	3.47
	L1M2*	2.473218e+02	1.07e+01	8.026	0.03709	0.238	3.09
	L2M4*	2.131887e+03	9.22e+01	8.102	0.31968	0.238	3.75
	L3N1*	3.650743e+01	1.58e+00	8.176	0.00547	0.239	3.66
	L1M3*	3.620914e+02	1.57e+01	8.231	0.05430	0.239	3.67
	L3N5*	6.763009e+02	2.92e+01	8.468	0.10141	0.240	3.06
	L1M4*	1.467439e+01	6.34e-01	8.598	0.00220	0.241	3.31
	L1M5*	1.370269e+01	5.92e-01	8.647	0.00205	0.241	3.10
	L2N1*	2.004631e+01	8.67e-01	9.145	0.00301	0.244	2.21
	L2N4*	5.948309e+02	2.57e+01	9.437	0.08919	0.246	1.12
	L2O1*	3.632108e+00	1.57e-01	9.564	0.00054	0.246	0.95
	L2N6*	1.296285e+00	5.60e-02	9.613	0.00019	0.246	1.39
	L1N2*	1.035178e+02	4.48e+00	9.730	0.01552	0.247	3.40
	L1N3*	1.471165e+02	6.36e+00	9.779	0.02206	0.247	4.52
	L1N5*	3.929739e+00	1.70e-01	9.936	0.00059	0.248	46.58
	L1O3*	3.455245e+01	1.49e+00	10.083	0.00518	0.249	262.33
Yb	L	2.352992e+04	3.31e+02				
	L3M1*	2.034707e+02	2.86e+00	6.546	0.00865	0.230	3.87
	L3M4*	7.786812e+02	1.10e+01	7.367	0.03309	0.234	3.16
	L3M5*	7.062149e+03	9.93e+01	7.416	0.30013	0.235	3.57
	L2M1*	1.408165e+02	1.98e+00	7.580	0.00598	0.236	3.30
	L2M3*	5.032697e+00	7.08e-02	8.028	0.00021	0.238	3.12
	L1M2*	8.755081e+02	1.23e+01	8.313	0.03721	0.240	2.93
	L2M4*	7.510428e+03	1.06e+02	8.402	0.31919	0.240	2.96
	L3N1*	1.306413e+02	1.84e+00	8.456	0.00555	0.240	3.03
	L1M3*	1.263030e+03	1.78e+01	8.537	0.05368	0.241	3.28
	L3N4*	2.372867e+02	3.34e+00	8.745	0.01008	0.242	2.62
	L3N5*	2.132693e+03	3.00e+01	8.759	0.09064	0.242	2.59
	L3O1*	2.426407e+01	3.41e-01	8.889	0.00103	0.243	2.58
	L1M4*	2.757946e+01	3.88e-01	8.910	0.00117	0.243	2.60
	L3N7*	7.203300e+00	1.01e-01	8.939	0.00031	0.243	2.67
	L1M5*	4.242905e+01	5.97e-01	8.959	0.00180	0.243	2.67
	L2N1*	6.894762e+01	9.70e-01	9.491	0.00293	0.246	1.13
	L2N4*	2.026965e+03	2.85e+01	9.780	0.08614	0.247	4.52
	L2O1*	1.226212e+01	1.72e-01	9.924	0.00052	0.248	38.65
	L2N6*	4.867361e+00	6.85e-02	9.973	0.00021	0.248	95.03
	L1N2*	3.522057e+02	4.95e+00	10.090	0.01497	0.249	264.26
	L1N3*	4.948548e+02	6.96e+00	10.143	0.02103	0.249	277.58

PyMCA : Advanced Fit Results

	L1N4*	5.370335e+00	7.55e-02	10.288	0.00023	0.250	322.49
	L1N5*	8.347889e+00	1.17e-01	10.301	0.00035	0.250	322.43
	L1O3*	1.148815e+02	1.62e+00	10.463	0.00488	0.251	369.05
Lu	L	1.290919e+04	3.60e+02				
	L3M1*	1.164580e+02	3.25e+00	6.753	0.00902	0.231	2.27
	L3M4*	4.308205e+02	1.20e+01	7.605	0.03337	0.236	3.07
	L3M5*	3.900542e+03	1.09e+02	7.656	0.30215	0.236	2.77
	L2M1*	7.975544e+01	2.23e+00	7.857	0.00618	0.237	3.22
	L2M3*	2.920861e+00	8.15e-02	8.325	0.00023	0.240	2.97
	L1M2*	4.682847e+02	1.31e+01	8.607	0.03628	0.241	3.36
	L2M4*	4.172811e+03	1.16e+02	8.709	0.32324	0.242	2.69
	L3N1*	7.175919e+01	2.00e+00	8.738	0.00556	0.242	2.65
	L1M3*	6.646625e+02	1.86e+01	8.847	0.05149	0.242	2.61
	L3N5*	1.284361e+03	3.58e+01	9.048	0.09949	0.243	2.69
	L3O1*	1.363543e+01	3.81e-01	9.187	0.00106	0.244	2.01
	L1M4*	2.513655e+01	7.02e-01	9.234	0.00195	0.244	1.77
	L1M5*	2.306280e+01	6.44e-01	9.282	0.00179	0.245	1.55
	L2N1*	3.740446e+01	1.04e+00	9.842	0.00290	0.248	8.55
	L2N4*	1.099560e+03	3.07e+01	10.144	0.08518	0.249	277.58
	L2O1*	6.806787e+00	1.90e-01	10.292	0.00053	0.250	322.49
	L2O4*	7.950083e+00	2.22e-01	10.344	0.00062	0.250	323.79
	L1N2*	1.819761e+02	5.08e+00	10.460	0.01410	0.251	370.26
	L1N3*	2.525542e+02	7.05e+00	10.511	0.01956	0.251	377.77
	L1N5*	7.295897e+00	2.04e-01	10.672	0.00057	0.252	200.13
	L1O3*	6.143659e+01	1.71e+00	10.842	0.00476	0.253	111.70
Hf	L	8.545040e+02	2.41e+02				
	L3M1*	8.049324e+00	2.27e+00	6.960	0.00942	0.232	2.44
	L3M4*	2.875682e+01	8.12e+00	7.844	0.03365	0.237	3.26
	L3M5*	2.601749e+02	7.35e+01	7.899	0.30447	0.237	3.35
	L2M1*	5.320834e+00	1.50e+00	8.139	0.00623	0.239	3.90
	L2M3*	2.040761e-01	5.76e-02	8.632	0.00024	0.241	3.18
	L1M2*	3.019617e+01	8.53e+00	8.905	0.03534	0.243	2.64
	L2M4*	2.837375e+02	8.01e+01	9.023	0.33205	0.243	2.78
	L1M3*	4.212406e+01	1.19e+01	9.163	0.04930	0.244	2.20
	L3N4*	8.431813e+00	2.38e+00	9.337	0.00987	0.245	1.42
	L3N5*	7.573188e+01	2.14e+01	9.347	0.08863	0.245	1.47
	L3O1*	9.269421e-01	2.62e-01	9.496	0.00108	0.246	1.11
	L3N7*	2.310613e-01	6.52e-02	9.544	0.00027	0.246	1.05
	L1M4*	1.977763e+00	5.58e-01	9.554	0.00231	0.246	1.01
	L1M5*	1.509029e+00	4.26e-01	9.609	0.00177	0.246	1.39
	L2N1*	2.450007e+00	6.92e-01	10.201	0.00287	0.249	286.57
	L2N4*	7.193884e+01	2.03e+01	10.516	0.08419	0.251	377.06
	L2O1*	4.552677e-01	1.29e-01	10.675	0.00053	0.252	187.17
	L2N6*	1.672760e-01	4.72e-02	10.722	0.00020	0.252	139.61
	L2O4*	8.380631e-01	2.37e-01	10.733	0.00098	0.252	133.71
	L1N2*	1.134309e+01	3.20e+00	10.834	0.01327	0.253	116.47
	L1N3*	1.552303e+01	4.38e+00	10.890	0.01817	0.253	84.39
	L1N4*	1.826153e-01	5.16e-02	11.047	0.00021	0.254	51.71
	L1N5*	2.846370e-01	8.04e-02	11.057	0.00033	0.254	48.38
	L1O3*	3.949059e+00	1.11e+00	11.237	0.00462	0.255	42.18
Scatter	Peak000	0.000000e+00	0.00e+00				
	Scatter 000	0.000000e+00	0.00e+00	13.500	1.00000	0.266	3.76
Scatter	Compton000	8.520174e+03	3.20e+02				
	Scatter 000	8.520174e+03	3.20e+02	13.153	1.00000	0.264	6.59

created: Mon Mar 03 14:16:22 2014

last modified: Mon Mar 03 14:16:22 2014 by mbexjja4